A THESIS SUBMITTED TO
THE GRADUATE SCHOOL OF NATURAL AND APPLIED SCIENCES
OF ÇANKIRI KARATEKİN UNIVERSITY

PREPARATION OF Ge NANOSTRUCTURES USING PULSED LASER ABLATION FOR TOXICITY GAS SENSOR DETECTION

IN PARTIAL FULFILLMENT OF THE REQUIREMENTS
FOR
THE DEGREE OF MASTER OF SCIENCE
IN
PHYSICS

BY

JAMAL ABID YOUSIF YOUSIF

ÇANKIRI

2023

PREPARATION OF Ge NANOSTRUCTURES USING PULSED LASER ABLATION FOR TOXICITY GAS SENSOR DETECTION

By Jamal Abid Yousif YOUSIF

July 2023

We certify that we have read this thesis and that in our opinion it is fully adequate, in scope and in quality, as a thesis for the degree of Master of Science

Advisor : Prof. Dr. Sebahaddin ALPTEKİN
Co-Advisor : Prof. Dr. Asmiet RAMIZY

Examining Committee Members:

Chairman : Prof. Dr. Şemsettin ALTINDAL
Physics
Gazi University

Member : Prof. Dr. Sebahaddin ALPTEKİN
Physics
Çankırı Karatekin University

Member : Prof. Dr. Çiğdem YÜKSEKTEPE ATAOL
Physics
Çankırı Karatekin University

Approved for the Graduate School of Natural and Applied Sciences

Prof. Dr. Hamit ALYAR
Director of Graduate School

I hereby declare that all information in this document has been obtained and presented in accordance with academic rules and ethical conduct. I also declare that, as required by these rules and conduct, I have fully cited and referenced all material and results that are not original to this work.

Jamal Abid Yousif YOUSIF

ABSTRACT

PREPARATION OF Ge NANOSTRUCTURES USING PULSED LASER ABLATION FOR TOXICITY GAS SENSOR DETECTION

Jamal Abid Yousif YOUSIF
Master of Science in Physics
Advisor: Prof. Dr. Sebahaddin ALPTEKİN
Co-Advisor: Prof. Dr. Asmiet RAMIZY
July 2023

Toxic gas sensors are instruments used to detect and quantify hazardous gas levels in the atmosphere. These sensors are commonly used in industrial and commercial settings where there is a risk of exposure to harmful gases. The sensor works by detecting the presence of the gas and providing an alert when the concentration reaches a dangerous level. In this work, nanostructures of germanium dioxide GeO_2 films were fabricated using pulsed laser ablation technology with laser wavelength 1064nm and laser energy 2000 mJ at different pulses (500, 1000, 1500, 2000, 2500). The structural and the optical properties were studied, and the sensitivity property was studied after deposition on quartz and silicon bases at 50 and 100°C. X-Ray diffraction (XRD) study showed that all (XRD) patterns have crystallized well, with three diffraction peaks related to GeO_2, hexagonal structure, and orthorhombic structure. The field emission scanning electron microscopy (FESEM) showed that the particle sizes ranged between 15-274 nm and the average particle sizes were 106, 140.9, 87.6, 81.68, and 117 nm. Absorbance and transmittance Ultraviolet-visible (UV-Vis) spectroscopy was used to investigate the optical characteristics of germanium dioxide films.

2023, 74 pages

Keywords: Electronic and optical properties, Germanium, Gas sensor, Nanostructures, Thin films

ÖZET

TOKSİSİTE GAZ SENSÖRÜ TESPİTİ İÇİN DARBELİ LAZER ABLASYONU KULLANARAK Ge NANOYAPILARININ HAZIRLANMASI

Jamal Abid Yousif YOUSIF

Fizik, Yüksek Lisans

Tez Danışmanı: Prof. Dr. Sebahaddin ALPTEKİN

Eş Danışman: Prof. Dr. Asmiet RAMIZY

Temmuz 2023

Zehirli gaz sensörü, ortamdaki zehirli gazların varlığını tespit etmek ve ölçmek için tasarlanmış bir cihazdır. Bu sensörler, zararlı gazlara maruz kalma riskinin olduğu endüstriyel ve ticari ortamlarda yaygın olarak kullanılır. Sensör, gazın varlığını algılayarak ve konsantrasyon tehlikeli bir seviyeye ulaştığında bir uyarı sağlayarak çalışır. Bu çalışmada, germanyum dioksit GeO_2 filmlerinin nanoyapıları, lazer dalga boyu 1064 nm ve lazer enerjisi 2000 mJ ile darbeli lazer ablasyon teknolojisi kullanılarak farklı darbelerde (500, 1000, 1500, 2000, 2500) üretilmiştir. Yapısal ve optik özellikler incelendi ve duyarlılık özelliği 50 ve 100°C'de kuvars ve silikon bazlar üzerinde biriktikten sonra incelendi. X-ışmı kırınım (XRD) çalışması, tüm XRD modellerinin GeO_2, altıgen yapı ve ortorombik yapı ile ilgili üç kırınım zirvesi ile iyi kristalleştiğini göstermiştir. Alan emisyon taramalı elektron mikroskobu (FESEM), parçacık boyutlarının 15-274 nm arasında değiştiğini ve ortalama parçacık boyutlarının 106, 140,9, 87,6, 81,68, ve 117 nm olduğunu göstermiştir. Germanyum dioksit filmlerinin optik özellikleri, absorbans ve geçirgenlik (UV-vis) spektrumu ölçülerek incelenmiştir.

2023, 74 sayfa

Anahtar Kelimeler: Elektronik ve optik özellikler, Germanyum, Gaz sensörü, Nanoyapılar, İnce filmler

PREFACE AND ACKNOWLEDGEMENTS

I thank Allah Almighty with incalculable thanks for his many and countless blessings, and I praise Him with a great thank you befitting the greatness of His majesty, generosity, favors and benevolence.

I would like to express my deepest gratitude to my thesis advisor, Prof. Dr. Sebahaddin ALPTEKİN and Prof. Dr. Asmiet RAMIZY, for their invaluable guidance and support throughout the entire research process. Their expertise and encouragement were instrumental in shaping this thesis and I could not have completed it without their mentorship.

Finally, I want to express my heartfelt appreciation to my family and friends for their unwavering support, love, and encouragement throughout my academic journey. Their belief in me has been a constant source of motivation and inspiration, in particular Dr. Abdulmuttalib Abdulkareem MUHSEN.

Thank you all for your contributions to this thesis.

Jamal Abid Yousif YOUSIF

Çankırı-2023

CONTENTS

ABSTRACT i
ÖZET ii
PREFACE AND ACKNOWLEDGEMENTS iii
CONTENTS iv
LIST OF SYMBOLS vii
LIST OF ABBREVIATIONS viii
LIST OF FIGURES ix
LIST OF TABLES xi
1. INTRODUCTION 1
2. LITERATURE REVIEW 4
2.1 Semiconductor 5
2.2 Doping Semiconductor 6
2.2.1 Passive type semiconductor (n-Type) 7
2.2.2 Positive-type semiconductor (p-type) 9
2.3 The Pulsed Laser Ablation in the Liquids 10
2.3.1 Laser ablation and particle formation 12
2.3.2 Laser-induced heating and melting 13
2.3.3 Explosive boiling 13
2.3.4 Evaporation 14
2.3.5 Plasma formation 14
2.3.6 Solid exfoliation 14
2.3.7 Hydrodynamic sputtering 15
2.3.8 Particle ejection (spallation) 15
2.3.9 Nucleation and condensation 16
2.3.10 Coagulation and agglomeration (Growth) 16
2.4 Mechanism of PLAL 17
2.5 Nanoparticles-Liquid Reaction 19
2.6 Nanotechnology 19
2.7 Nanostructures 20
2.8 Germanium (Ge) 21

2.8.1 Germanium metal 21
2.8.2 Germanium nanoparticles 22
2.8.3 Applications of Ge 24
2.9 Gas Sensors 26
2.9.1 Fundamental parameter of gas sensor 27
2.10Response Mechanism 29
3. MATERIALS AND METHODS 32
3.1 Diffraction of X-rays (XRD) 32
3.2 Electron Microscopy Scanning 33
3.3 UV-Visible Spectroscopy 33
3.4 Liquid-Based Laser Ablation 35
3.4.1 The source of laser 36
3.4.2 Cell holder 36
3.5 Chemical Thermal Spraying 37
3.6 Substrate Preparation 38
3.6.1 Quartz substrate 38
3.6.2 Silicone substrate 38
3.7 Prepare Germanium Nanoparticles 38
3.8 Deposition of Thin Films 39
3.9 The Measurement Techniques 40
3.9.1 Device for X-ray diffraction 40
3.9.2 Utilizing SEM (scanning electron microscopy) 40
3.9.3 A UV-visible spectrophotometer 41
3.9.4 Gas sensor 41
4. RESULTS AND DISCUSSION 43
4.1 The Analysis of X-Ray Diffraction (XRD) 43
4.2 Optical Properties 45
4.2.1 Absorption spectra 45
4.2.2 Optical energy gap 46
4.2.3 Transmittance (T) 49
4.2.4 The absorbance coefficient 50
4.2.5 Coefficient of extinction (k) 52

4.2.6 The real and the imaginary part of dielectric constant (εr, εi) 53
4.3 FESEM Measurement of Ge Structures 55
4.4 Gas Sensor Results 58
5. CONCLUSIONS AND RECOMMENDATION 64
5.1 Conclusions 64
5.2 Recommendation 65
REFERENCES 66
CURRICULUM VITAE .... Hata! Yer işareti tanımlanmamış.

LIST OF SYMBOLS

A	Absorbance value
IA	Absorbed intensity
Å	Angstrom value
Cs	Crystal size
℃	Degree celsius
eV	Electron volt
E_g	Energy gap
GaAs	Gallium arsenide
R_g	Gas sensitivity
Ge	Germanium
NCs	Nanocrystals
NPs	Nanoparticles

LIST OF ABBREVIATIONS

DLC	Diamond-like carbon
EDS	Energy dispersive X-ray spectroscopy
FESEM	Field emission scanning electron microscope
GeOI	Germanium-on-insulator
LED	Light-emitting diode
LCD	Liquid-crystal display
PLAL	Pulsed laser ablation in liquids
SEM	Scanning electron microscopy
UV-VIS	Ultraviolet-visible
XRD	X-Ray diffraction

LIST OF FIGURES

Figure 2.1 Doping semiconductor silicon with (n-type) impurities (Siu 2022) 8
Figure 2.2 The energy bands in a semiconductor are of the negative type (n-type) (Siu 2022).......... 9
Figure 2.3 Doping semiconductor silicon with positive-type impurities (Siu 2022) . 9
Figure 2.4 The energy bands in a semiconductor are of the (p-type) (Bott 1998) ... 10
Figure 2.5 Steps to synthesis nanomaterials through the laser ablation process (Amendola and Meneghetti 2013).......... 12
Figure 2.6 Material removal via vaporization (left), pressure-induced melt displacement (middle), and explosive melt ejection (right).......... 16
Figure 2.7 Timeline and mechanism of the PLAL (Xiao *et al.* 2017).......... 18
Figure 2.8 Electronic density states and quantum confined systems as a function of the dimension.......... 21
Figure 2.9 Response time and relaxation time (Chen 2010) 29
Figure 2.10 (a) The n-type semiconductor membrane undergoes gas-phase oxygen adsorption (b) The electrons are returned to the membrane after oxygen is removed via the reducing gas reaction (CO) (Ozdemir 2011) 31
Figure 3.1 Diffraction by X-rays. crystal structure, Bragg's law, and the X-ray diffraction pattern are shown below (Lehn 1993).......... 33
Figure 3.2 The experimental procedure as a flowchart 35
Figure 3.3 Laser ablation in liquid Ge Nps.......... 36
Figure 3.4 Thermal chemical spray system.......... 37
Figure 3.5 Schematic diagram of laser ablation set-up of Ge NPs.......... 39
Figure 3.6 Typical gas sensor setup.......... 41
Figure 3.7 Components of the gas sensor.......... 42
Figure 4.1 XRD pattern of Ge prepared with Pulse number (500, 1000, 1500, 2000, 2500).......... 45
Figure 4.2 Ge nanoparticle absorption spectra for a range of laser pulse intensities (500, 1000, 1500, 2000, 2500) 46
Figure 4.3 The energy gap for Germanium at the number of pulses 500.......... 47
Figure 4.4 The energy gap for Germanium at the number of pulses 1000.......... 47
Figure 4.5 The energy gap for Germanium at the number of pulses of 1500.......... 48
Figure 4.6 The energy gap for Germanium at the number of pulses 2000.......... 48
Figure 4.7 The energy gap for Germanium at the number of pulses 2500.......... 49
Figure 4.8 The transmittance spectra of Ge nanoparticles with different laser pulse numbers (500, 1000, 1500, 2000, 2500).......... 50
Figure 4.9 The absorbance coefficientof Ge nanoparticles with different laser pulse numbers (500, 1000, 1500, 2000, 2500).......... 51
Figure 4.10 The effect of changing the number of laser pulses on the refractive index (n) of Ge nanoparticles (500, 1000, 1500, 2000, 2500) 52

Figure 4.11 Ge nanoparticles' extinction coefficient (k) as a function of laser pulse number (500, 1000, 1500, 2000, 2500) 53
Figure 4.12 Real part of dielectric constant (εr) of Ge nanoparticles with different laser pulse numbers (500, 1000, 1500, 2000, 2500) 54
Figure 4.13 Imaginory part of dielectric constant (εi) of Ge nanoparticles with different laser pulse numbers (500, 1000, 1500, 2000, 2500)................. 54
Figure 4.14 The microscopic images of Ge nanoparticles of 500 pulsed................... 55
Figure 4.15 The microscopic images of Ge nanoparticles of 1000 pulsed................. 56
Figure 4.16 The microscopic images of Ge nanoparticles of 1500 pulsed................. 56
Figure 4.17 The microscopic images of Ge nanoparticles of 2000 pulsed................. 57
Figure 4.18 The microscopic images of Ge nanoparticles of 2500 pulsed................. 57
Figure 4.19 Change of sensitivity as a function of time at 500 pulses at temperatures of 50 and 100°C 59
Figure 4.20 Change of sensitivity as a function of time at 1000 pulse at temperatures of 50 and 100°C 59
Figure 4.21 Change of sensitivity as a function of time at 1500 pulse at temperatures of 50 and 100°C 60
Figure 4.22 Change of sensitivity as a function of time at 2000 pulse at temperatures of 50 and 100°C 60
Figure 4.23 Change of sensitivity as a function of time at 2500 pulse at temperatures of 50 and 100°C 61
Figure 4.24 Sensitivity as a function of the number of the pulse at temperatures of 50 and 100°C 62
Figure 4.25 Response time as a function of the number of pulses at temperatures of 50 and 100°C 62
Figure 4.26 Recovery time as a function of a number of pulses at temperatures of 50 and 100°C 63

LIST OF TABLES

Table 4.1 Structural properties of the prepared films 44
Table 4.2 Value of energy gap for germanium at different pulsed laser number.... 49
Table 4.3 Values of sensitivity, response, and recovery time 61

1. INTRODUCTION

There may be chances to develop better goods and materials thanks to nanotechnology. Both directly employing nanomaterial to detect, prevent, and remove pollutants as well as indirectly using nanotechnology to develop more environmentally friendly industrial processes and produce environmentally friendly goods are two ways that nanotechnology may help the environment. About 100.000 times smaller than the diameter of a human hair and 1,000 times smaller than a red blood cell, a nanometer is equivalent to 10^{-9} meters (Morris and Willis 2007). The classical laws of physics and chemistry do not readily apply at this very small scale for two reasons. Firstly, the electronic properties of very small particles can be very different from their larger cousins. Secondly, the ratio of surface area to volume becomes much higher and since the surface atoms are generally most reactive, the properties of a material change in unexpected ways (Al-Maher *et al.* 2021). Size, shape, and composition are the main factors that affect the physical and chemical characteristics of metallic nanoparticles. Thus, it is crucial to manage these variables in order to modify the nanoparticles' characteristics. Controlling the form has received a lot of attention recently since it makes it possible to fine-tune optical qualities more versatilely than is possible otherwise. The ability to manipulate the form of metal nanoparticles created in solution very lately has allowed for the creation of several synthetic techniques (Naskar *et al.* 2017).

Soon after the creation of the pulsed ruby laser in the 1960s, pulsed laser ablation was first created. The production of nanomaterials and the creation of nanostructures have both benefited greatly in recent decades through the widespread usage of laser ablation of a solid target in a liquid environment. Pulsed laser ablation has received a lot of attention lately since it can be used to create thin films (Franklin and Thareja 2005). The manufacture of pure nanoparticle colloids free from contaminants brought on by chemical precursors or preservatives is possible thanks to pulsed laser ablation in liquids (PLAL) (Dahl *et al.* 2007). Semiconducting nanoparticles are highly suited for devices that produce energy as well as biological and environmental sensors. Most of the research to date has been on II-VI semiconductor systems with systematically varying bandgaps and luminous characteristics. Nonetheless, Ge nanoparticles have a wide range of uses, including as precursors for the creation of thin films. Chiu *et al.* (2006), for porous germanium (Ge) (Shieh *et al.* 2004), and for probes, independent of the source of light output. Due to their distinct size-dependent properties that differ greatly from those of bulk materials, nanoparticles, and nanocrystals are of tremendous interest in the study of materials physics (Yoon *et al.* 2005). In comparison to the bulk material, the electrical characteristics of the semiconductor nanoparticles alter. For instance, the band gap increases as the particle size decreases. By adjusting the particle size, we can alter the material's electrical characteristics (Trindade *et al.* 2001). One of the most interesting fields of semiconductor research and technology is the study of semiconductor nanoparticles, often known as quantum dots. Given its straightforward methodology, the laser ablation method was used in this research to create Ge nanoparticles (Huang *et al.* 2002).

Gas sensors fabricated from thin films of semiconductors, such as metal oxides, are used in many different industrial and life fields. These sensors are relatively inexpensive compared to other sensor technologies, with high stability, small size, and fast responsivity. It is used in many fields to detect and monitor harmful gases even if they are in small quantities, especially harmful gases such as carbon oxide and nitrogen dioxide. Sensors made using nano-clusters are promising due to the large surface area of cluster films as well as potential control over the surface morphology of devices by selecting the cluster size. Previous work in our group has demonstrated that films of percolating tin oxide nano-clusters can be used as ammonia sensors and hydrogen sensors (Fine *et al.* 2010, Lassesson *et al.* 2007).

The aim of this study.

The following experimental effort is done to achieve the aims of the creation of efficient devices:

- Preparation of Ge nanoparticles by Pulsed Laser Ablation Liquids (PLAL) technique from Ge Plate with constant energies

- Preparation of thin films from germanium nanoparticles by a cost-projection method on a layer of silicon n-type (111) and study of the effect of the Change PLAL on the structural optical, and sensitivity properties of Ge thin films and Research the impact of response time on other qualities, including structural, optical, and sensitivity properties, as well as sensing behaviour.

2. LITERATURE REVIEW

In 2005, Davydov (2005) investigated the atomic hydrogen adsorption on Ge (100) and Ge (111) surfaces, and found that the work function grows at Q 0.1, while the value of (Q) is negative at Q 0.15 and positive at Q > 0.15(Davydov, 2005).

In 2012, Mackenzie and Brown (2012), fabricated films of germanium nanoclusters of 30 nm diameter in a high-vacuum deposition apparatus. The resistance increase was accelerated when exposed to dry air but decreased when exposed to ambient air. The films were sensitive to hydrogen concentrations above 1% in dry air, but only observed at temperatures below 100℃. Surface moisture is necessary for films to show sensitivity to hydrogen.

Thin sheets of germanium-zinc silicate (Ge/Zn_2SiO_4) were fabricated in an extremely hot oven, investigated by scanning electron microscopy, energy-dispersive X-ray spectroscopy, and X-ray diffraction. Nickel MSM contacts were deposited on the film, demonstrating photosensitivity and potential for gas sensor devices (Jumidali *et al.* 2013).

Al-Dahan and Abduljabbar (2013), their studied found that n-type germanium samples were doped with boron and subjected to laser irradiation with an Nd: YAG laser with a wavelength of 1064 nm at various intensities. The rise time ranged from 83 to 75 ns.

Vadavalli *et al.* (2014) found that when the energy of the laser pulse increases, the mean size of the Ge nanoparticles changes from a few nm to 40 nm. The crystalline nature of the created nanoparticles is confirmed by high-resolution TEM and micro-Raman spectroscopy, and there is good agreement between the observed NP sizes from the micro-Raman phonon quantum confinement model and TEM observations.

Hadi (2015) The work presents the fabrication and liquid technique for the characterization of germanium (Ge) nanoparticles using pulsed laser ablation (PLAL) at different laser fluences. Atomic Force Microscopy, Energy Dispersive Analysis of X-rays, and Spectrophotometers were used to study the surface and sizes of the nanoparticles. UV-visible measurements showed a variation in the energy gap in the absorption spectra with increasing laser fluence. Controlling the irradiation conditions allows for particles of different diameters and changes the electronic properties of the material.

Samà *et al.* (2016) fabricated Ge nanowires with Au catalyzed Vapor Liquid Solid (VLS) mechanism and tested them with water vapor in synthetic air. Results showed reproducible responses towards H_2O, with resistance increasing with increasing relative humidity. Response time was 10 minutes.

Wang *et al.* (2017) the GeS monolayer is sensitive to NO_2 molecules with moderate adsorption energy and charge transfer, with a sorption quantity of 708.707 mg/g under 101.33 kPa. This suggests it is a potential sensing material for NO_2 gas.

Dong *et al.* (2018) report a NO_2 gas sensor based on germanium quantum dots (GeQDs)/graphene hybrids with improved sensitivity to NO_2, fast response and recovery rates, and excellent stability. This work may provide a new route to mass production.

Pasanen *et al.* (2020) the nanostructured Ge wafers can increase the sensitivity of Ge sensors by up to 99% in the UV–vis–NIR spectrum. This process is applicable to CMOS sensor manufacturing and could revolutionize the sensitivity of Ge-based sensors.

Hirose *et al.* (2021) a nanostructured Si-Ge thermoelectric material is used to create a high-performance sensor that detects infrared rays and methane.

2.1 Semiconductor

Materials are classified in nature in terms of their electrical conductivity at room temperature into conductive materials, which have the high electrical conductivity in the range of (10^{-8}-10^{-18}) $\Omega.cm$, and insulators with low conductivity very within (10^{-3}-10^{-8})

$\Omega.cm$, and semiconductor materials have a conductivity in the range of (10^3-10^8) $\Omega.cm$, as their conductivity lies between the conductive and insulating materials These semiconductor materials are insulators at low temperatures, but when their temperature is raised, they will have the ability to conduct electricity, as the density of electrons available for conduction increases with increasing temperature and the electrons are stimulated, leading to the energy of the forbidden gap, and the conduction of semiconductors can be controlled by heat (Khoudro and Najeeb 2020). The advantages of semiconductors can be summarized in the following points (Tribble 2002).

- A semiconductor of extremely high purity exhibits self-conductivity and has a Fermi level in the center of the energy gap.
- Semiconductors have a resistance with a negative thermal coefficient, meaning that the dependence of their electrical conductivity on temperature is opposite to that of metals, as the resistance of a semiconductor decreases with increasing temperature.
- It has a specific resistance between (10^3-10^8) $(\Omega.cm,)^{-1}$
- Semiconductor materials are sensitive to light, meaning that the resistance of the semiconductor changes upon exposure to light of an effective wavelength.
- Its conductivity is affected when a magnetic and electric field is applied to it.
- The thermoelectric capacity generated by these materials is high compared to that generated by metals.
- Semiconductors have either positive electrical conductivity (P) or negative electrical conductivity (n).
- Impurities may change the conductivity of a semiconductor from donor to acceptor and vice versa.

2.2 Doping Semiconductor

Doping refers to the practice of introducing impurities into an otherwise unaltered intrinsic semiconductor in order to modify its behavior. Due to an equilibrium between electrons and holes in the conduction and valence bands at room temperature, the conductivity of these materials is low. The extinction of competing carrier types (Willardson *et al.* 1991).

The doping process is the best way to control the conductivity of semiconductors compared to the thermal effect coefficient because the increase in temperature is undesirable in electronic applications (Bowen and Tanner 2005). Two types of semiconductor materials can be distinguished, after doping them by certain elements of the periodic table (three and five valences) and the following is a description of these two types.

2.2.1 Passive type semiconductor (n-Type)

Semiconductor materials doped with the elements of the fifth group in the periodic table are called semiconductors (P) such as silicon when doped with the element phosphorous (n-type) conductors of the negative type when adding a known amount (Donors). These elements are called donor elements (As) arsenic from one of these elements which have five valence electrons, will enter into the composition of the semiconductor material and form covalent bonds with the surrounding atoms, for example, when each impurity atom generates an additional electron when (Si) as an impurity to silicon (P) added by phosphorous, four electrons from the impurity atom combine with four electrons from the silicon atom to create a covalent bond, leaving one electron attached to the parent atom. as shown in Figure 2.1 (Siu 2022).

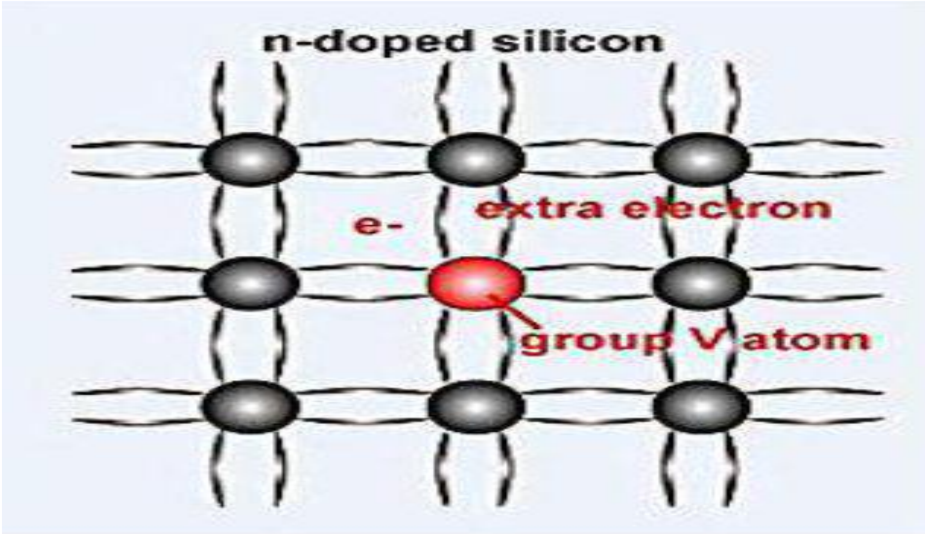

Figure 2.1 Doping semiconductor silicon with (n-type) impurities (Siu 2022)

Therefore, separating this electron from the atom does not require much energy, while it requires much less energy to transfer it from the valence bundle to the conduction bundle. Due to the presence of impurities, the appearance of excess electrons in the conduction band does not coincide with the appearance of holes in the valence band, and these electrons do not move out of the valence band as in a pure substance. But it moves from the states located below the edge of the conduction beam, these states are local levels, called donor levels, and at a very small depth represent the energy required to liberate electrons from the impurity atoms (Siu 2022). The density of states located below the edge of the beam represents the density of impurity atoms, while the density of the gaps depends on the electrons leaving from the valence bundle to the conduction bundle so that it is few, so the current flowing here is transferred by electrons in a basic degree, as shown in the Figure 2.2. Electrons are called majority carriers, and gaps are called minority carriers so that their effect on electrical conduction is negligible (Bott 1998).

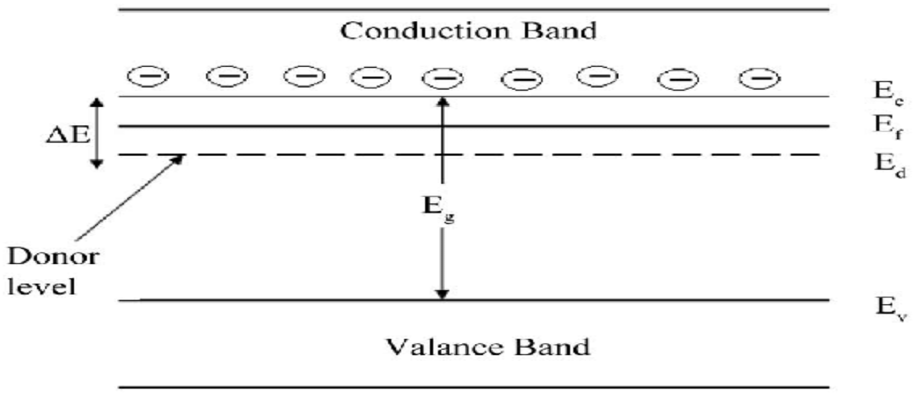

Figure 2.2 The energy bands in a semiconductor are of the negative type (n-type) (Siu 2022)

2.2.2 Positive-type semiconductor (p-type)

A semiconductor doped with a known amount of the third group of elements of the periodic table, such as aluminum (Al) or boron (B), is called a p-type semiconductor, in which the holes are replaced instead of electrons. (Si), the aluminum atoms will occupy the places of the silicon atoms and bond to the four atoms. A covalent bond surrounding each of them, since the impurity contains three electrons in its shell, there will remain one covalent bond containing one electron, and as shown in the Figure 2.3 (Siu 2022).

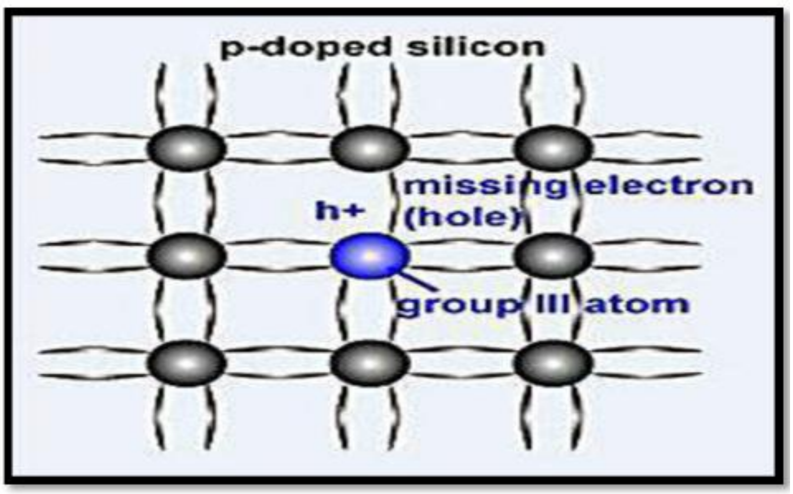

Figure 2.3 Doping semiconductor silicon with positive-type impurities (Siu 2022)

In this case, the impurity atom can easily take an electron from its neighboring bonds and thus complete its bonds, but this will leave a positive gap in those bonds. From one of the bonds of the semiconductor material and placing it in one of the bonds formed between the atoms of the impurity semiconductor which are very small, and the gaps here are called the majority carriers, as shown in Figure 2.4 (Bott 1998).

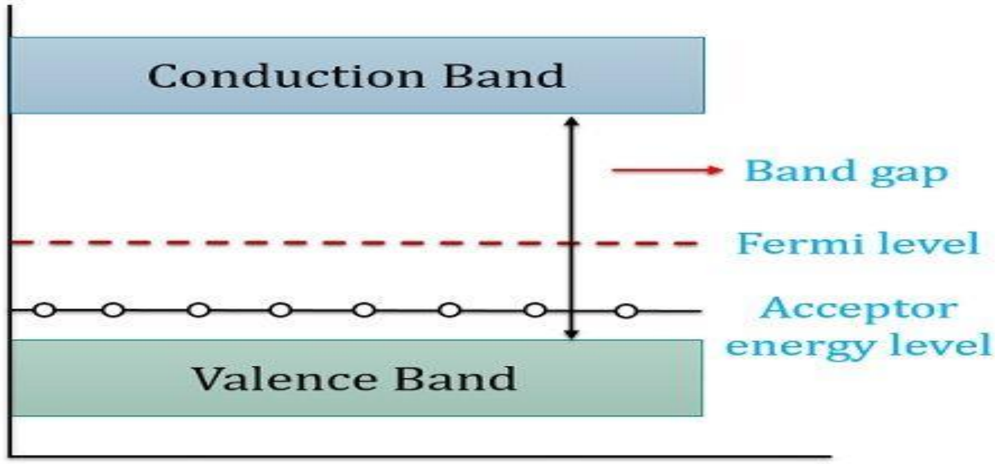

Figure 2.4 The energy bands in a semiconductor are of the (p-type) (Bott 1998)

2.3 The Pulsed Laser Ablation in the Liquids

Synthesis of nanomaterials may be accomplished quickly, easily, and environmentally friendly using pulsed laser ablation in liquid solutions (PLAL). Little equipment is needed for the PLAL approach. The fact that PLAL's products are chemically pure is their biggest benefit. Many products, including Ag, Au, Ge, and Cu nanoparticles, alloy nanoparticles, heterostructures, nanocubes, nano-spindles, noble metal core/shell nanostructures, and metal/metal oxide semiconductor core/shell nanostructures, have reportedly been produced using PLAL. While PLAL is of great value in the synthesis of nanostructures, it must be integrated with chemical processes for the synthesis of metal and oxide core/shell nanostructures containing two different elements (Zhao *et al.* 2015). In PLAL, a focused laser beam is used to irradiate a solid target that is submerged in a liquid medium inside the reactor. The ablation plume, which is composed of atoms, ions, molecules, clusters, and particles, is created when the beam strikes the surface of the solid target and vaporises it. Nanostructures including atoms from both the initial target and the liquid are created when the intermediate reactive products in the plume interact with the molecules of the surrounding liquid. A favorable environment for the creation of metastable phases and the promotion of the synthesis of diverse nanostructures is provided by confinement created by the liquid layer in conjunction with the high temperature and high pressure caused by the focussed pulsed beam (Ali 2010). Both laser ablation in a hoover and laser ablation at the solid-liquid interface follows a similar process of laser interaction with the target. Both generate plasmas and strong emission species confinement, which facilitates effective electron-ion recombination. When the plasma starts to expand, it does so freely in a vacuum but is constrained by any liquid layer. Here is where the difference arises. The liquid slows down the plasma's growth, creating a high plasma pressure and temperature that promotes the synthesis of new materials. Another benefit is that because both the liquid and the solid targets are vaporised, the final product may contain atoms from both the liquid and the target material (Wang *et al.* 2002). Pulsed laser ablation in a liquid media (PLAL) has recently been used for nanoparticle and nanocomposites preparation. This can be accomplished by fine-tuning the laser fluence and ablation time (Vinod and Gopchandran 2015). The interaction of high-energy laser radiation with a solid surface can produce many physical processes. These processes include absorption of laser radiation by a solid target, thermal conduction into the target, vaporization, and diffusion of target material, the rapid heating of the target, and subsequent plasma formation leading to vaporization of the fluid and the formation of a cavitation bubble. Nanomaterial (nm) nucleation and growth occur in the later stages as shown in Figure 2.5 (Amendola and Meneghetti 2013).

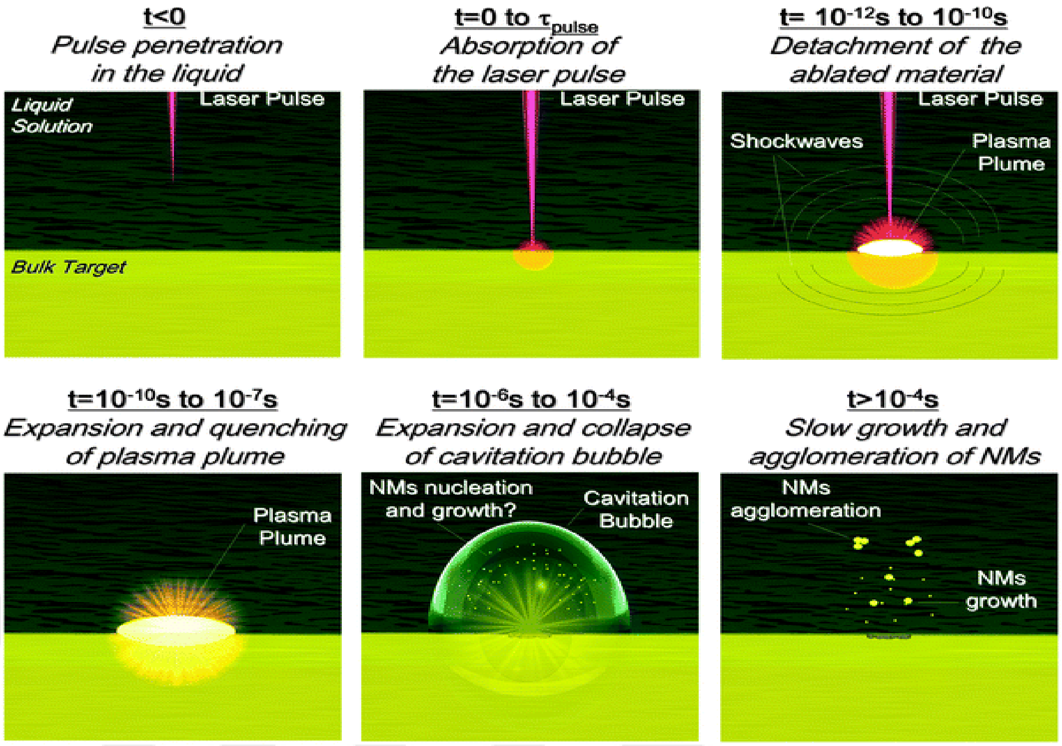

Figure 2.5 Steps to synthesis nanomaterials through the laser ablation process (Amendola and Meneghetti 2013)

2.3.1 Laser ablation and particle formation

A laser pulse's energy is partially reflected when it hits a sample. Keep in mind that reflectivity is influenced by both the material and the laser wavelength. The sample absorbs energy after it has been transferred from optical photons to electrons and then to the lattice, where it is diffused into the material. Photochemical processes triggered by exceptionally high-energy pulses have the potential to strip the surface of its atoms and molecules. When the surface temperature of a heat source approaches the critical point, rapid evaporation may occur. Vaporization results in plasma, which is composed of ionized vaporized atoms and electrons. The plasma cloud may absorb some of the incident laser energy, preventing it from reaching the surface (plasma shielding). The plasma expands and heats up as a result of absorbing photons. Later, as the vapour cools, aerosol particles begin to form. The leftover energy is absorbed by the material as heat. If enough laser energy is applied, the surface of a moving solid-liquid contact can melt into the liquid below. It's possible that the ablation rate might be increased byremoving tiny droplets of the liquid from the molten pool.

2.3.2 Laser-induced heating and melting

Absorption of laser light by metal nanoparticles triggers a chain reaction of energy transformation activities. These include electron-phonon relaxation and phonon-phonon thermalization, respectively, as well as the following excitation and relaxation of metal electrons and their interaction with the lattice. After that, other kinds of melting and evaporation might occur, among other heat reactions. As was indicated before, in the case of nanosecond-pulsed laser light, the time scale during which heat diffusion happens from the metal particle to the support is substantially shorter than the pulse width. As a result, the increase in temperature caused by the laser can be countered using only the principles of thermodynamics. The laser energy does not cause the material to vaporize, but rather heats it to a higher temperature and causes it to radiate heat throughout (Liu 2005, Zimmer 2009).

2.3.3 Explosive boiling

When a laser pulse with a very high energy fluence is applied to a surface, the crater's volume and shape are dramatically altered. The ablation rate, measured by the depth of the crater, changes dramatically as the energy power density exceeds a particular threshold. Thermodynamic principles from the past have been used to analyze this procedure. When the surface region is heated above the limit of its thermodynamic stability during short-pulse laser irradiation, the transition from a superheated liquid to a combination of vapour and liquid droplets is predicted to occur swiftly. Experimental results showing a threshold fluence for the onset of droplet ejection and a dramatic increase in the ablation rate at the threshold have been published and interpreted by researchers as evidence of the transition from conventional vaporization to phase explosion.

2.3.4 Evaporation

Evaporating mass from a target at high temperatures and pressure results in a plume of vapour that rises and moves away from the surface. The rate of evaporation is controlled mostly by the temperature of the surface (Liu 2005).

2.3.5 Plasma formation

The portion of the target surface that came into contact with the laser quickly heated up to extremely high temperatures. Much of the absorbed laser energy is used to vaporize the atoms of the target material, reducing the quantity of energy carried into the interior of the target material. When the front of the vapor-formed plasma collides with the surrounding material at a speed greater than the speed of sound, a shockwave is produced. The vapour plasma has a density of 16 ions, which is in the range of 10^{16}–10^{18} ions/cm^3, indicating a severe nonequilibrium situation. The typical time for cloud formation is around 107 seconds. Internal plasma temperatures can soar into the tens of thousands of Kelvin when all atoms and molecules have been ionized (Li *et al.* 2003, Zhigilei *et al.* 2009).

2.3.6 Solid exfoliation

Photomechanical processes caused by strong thermal expansion and tension induced by lasers lead to exfoliation, the removal of fragmented material from a solid state. This kind of removal is critical for materials like silicon, graphite, and glasses, which are brittle and refractory but can be broken if they are not removed. Under stress confinement conditions, the amplitude of the laser-induced stresses becomes significant when the duration of the laser pulse is shorter than the time required for the absorbing volume to mechanically rebalance. Particles tend to break along the crystallographic planes. The particles are large and uneven. The crater's shape makes it easy to identify the sample's surface after the exfoliation process (Liu 2005).

2.3.7 Hydrodynamic sputtering

Transient melting and motion of a liquid due to strong temperature gradients and laser-induced pressure relaxation results in the ejection of large droplets. Hydrodynamic sputtering is a common phenomenon that occurs in a wide variety of processes. Although it is easy to recognize particles that are evacuated while they are still liquid, the liquid could depart the surface by a number of different ways. Hydrodynamic sputtering is a common phenomenon in laser ablation due to the cyclic heating and cooling of the surface. After the surface has been sufficiently burned by the laser, surface patterns resembling fingers or ridges appear as a result of repetitive heating and cooling of the surface, which causes perturbations to rise. Droplets of liquid can break off of a molten layer if an asperity, or protrusion, induced by thermal expansion moves at a pace greater than the force keeping it anchored (Povarnitsyn *et al.* 2009).

2.3.8 Particle ejection (spallation)

The particles' spherical form proves that they originated in a liquid condition. The liquid-solid interface is where the big particles are created. The laser-induced strains may be greater than the target material's dynamic tensile strength in the domain of stress confinement, disrupting the liquid-solid interface. When a target material is rapidly heated and vaporised by a high-energy laser pulse, a thermomechanical strained condition is created. The frontal cavitation of the subsurface layer might result from its unloading. When the rarefaction wave created by the compression wave reaches the back of the target, it destroys it. The latter has the potential to cause spallation and cracking in the back. But the evaporating substance released a cloud of vapor that drifted out into the distance. The plume's pressure and temperature are highest during the beginning of the vapourization process. Extreme pressure might force liquid melt out of the center of the laser-heated zone, creating a volcano-like crater when the melt cools (Figure 2.6). When the pressure is high enough, the droplets are expelled because their momentum is greater than the surface tension holding the liquid in place (Fishburn *et al*. 2006, Liu 2005, Zhakhovskii *et al.* 2009, Zhigilei *et al.* 2009).

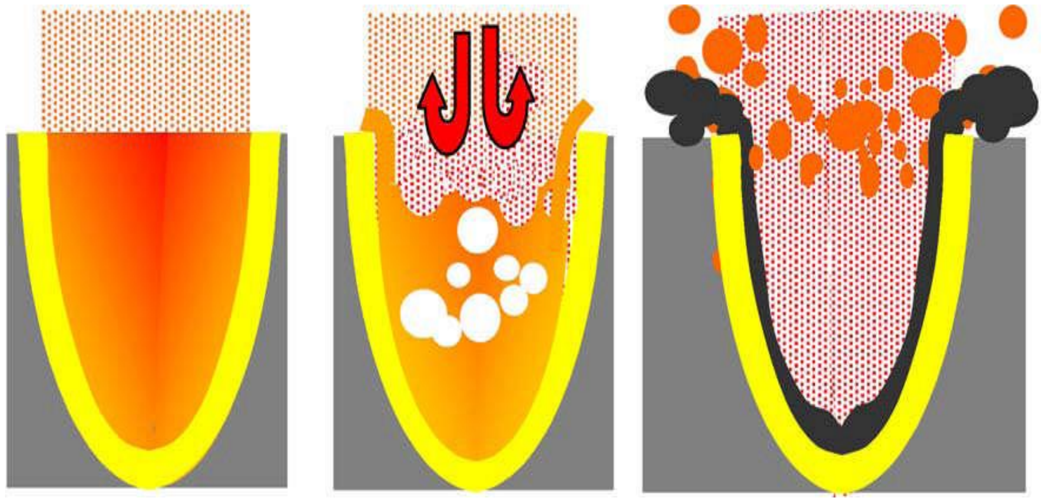

Figure 2.6 Material removal via vaporization (left), pressure-induced melt displacement (middle), and explosive melt ejection (right)

2.3.9 Nucleation and condensation

As the vapor plume extends and starts to cool, the colder front of the plume cloud allows aerosol particles to develop. The typical characteristic time for particle generation is on the order of nanoseconds (10^{-9} sec), which is orders of magnitude shorter than the lifetime of the cloud. Due to the significantly shorter time scale for particle creation, the vapor will be transformed into particles. Condensation of evaporated atoms is the process that results in Nano-sized particles. The ambient pressure, gas properties, and temperature all play crucial roles in condensation processes. Most numerical studies of this process have involved calculating the location of the shock and the properties of the gasoline. Condensation processes were predicted to begin once the plasma temperature fell to a value below the vapour number density. Because of the need for extremely high collision frequencies and atom number densities, the formation of micron-sized particles is extremely improbable (Liu 2005, Noël *et al.* 2009).

2.3.10 Coagulation and agglomeration (Growth)

There are several secondary actions that, while not directly creating particles, may alter the particle size distribution or the overall particle concentrations. Coagulation, for example, can begin anywhere from a few nanoseconds to a few milliseconds after the laser pulse. The two most important processes were coagulation and agglomeration, both of which contributed to the ultimate particle size increasing. Particles develop via laser ablation and then collide with one another in a gaseous medium. Particles can merge to form new, larger particles if they are in a liquid state or have enough momentum. The latter phases of development are characterized by an activity known as coagulation. Condensation triggers the formation of agglomerates of nanoscale aerosols, which are highly charged with electrons from plasma. Once that happens, the charged particles are connected electrically (Tsuji *et al.* 2008).

2.4 Mechanism of PLAL

PLAL has many desirable advantages. It is a simple one-step process and an effective technique to prepare nanoparticles in large amounts suspended in liquid (Kazakevich *et al.* 2006). The ablation process is conducted in an ambient environment that does not require high pressure or temperature. The PLAL production system is low cost and has simple starting materials, chemically simple, and no catalyst is needed. These factors ensure the production of ultra-pure, clean surface nanoparticles that may have high surface activity (Xiao *et al.* 2017). A broad variety of nanoparticle formations is produced by PLAL, which is difficult to do using conventional procedures. Last but not least, it offers a practical method for altering the physical characteristics of the laser, such as its power, wavelength, repetition rate, focusing situation, pulse duration, and a number of pulses, or the characteristics of the liquid, such as its kind, PH level, and surfactant (Darwish *et al.* 2016).

The solid target continues to absorb laser radiation, creating more vaporized species, which expands the plasma plume, creating a shockwave with high temperature and pressure. This pressure is called plasma-induced pressure and helps to further raise the temperature, density, and pressure of laser-induced plasma (Amendola and Meneghetti 2013).

A thin layer of vapor with high temperature is created due to energy transfer from plasma to the surrounding liquid during the plume expansion and condensation, creating cavitational bubbles. The vapor expands and transforms into bubbles with a radius larger than the vapor layer. The pressure inside the bubbles is increased by liquid confinement (Darwish *et al.* 2016). The plasma plume cools down after transferring its energy to the vapor layer. This leads to bubbles expanding in every direction moving against the liquid and the compressed plasma. Then, the bubbles' internal pressure balances with the surrounding liquid gradually and reaches the maximum radius. The bubbles maintain this state for some time. Finally, it collapses and nanoparticles are released into the liquid. Nanoparticles are produced during plasma shrinking. They originate from reacting liquid medium and target molecules. Afterward, they diffuse in the cavitational bubbles and then finally released into the solution (Xiao *et al.* 2017). Figure 2.7 shows the steps involved in the PLAL procedure.

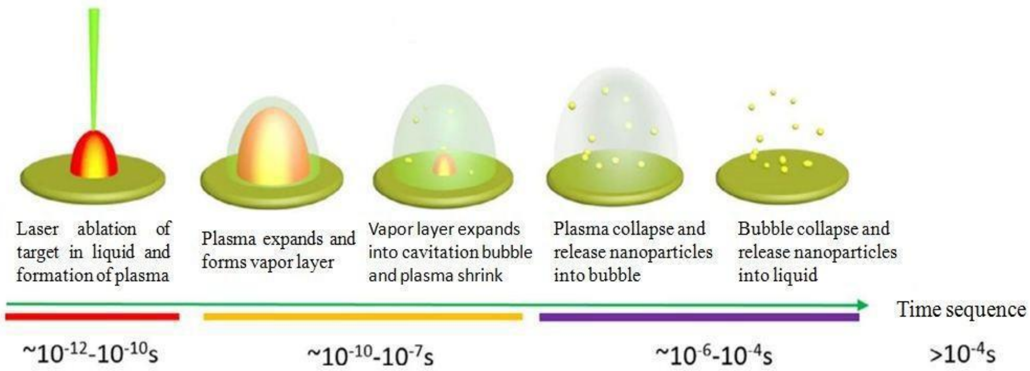

Figure 2.7 Timeline and mechanism of the PLAL (Xiao *et al.* 2017)

At the liquid and plasma induced by laser interface, four chemical reactions are happening during plasma transformation (Amendola and Meneghetti 2013, Xiao *et al.* 2017, Zhang *et al.* 2017).

- Within the laser-induced plasma, the ablated target species react with metastable phases created by the plasma's extreme conditions of high temperature, pressure, and density.
- The laser-induced plasma undergoes a chemical reaction as well, but this time it's between the target's ablated species and the excited liquid molecules.

- There is a good probability for high-temperature chemical interactions between the liquid molecules and the ablated target species at the liquid and laser-induced plasma interface due to the high temperature, density, and pressure of the laser-induced plasma.
- Molecules of the liquid undergo a chemical interaction with the ablated target species. Nanoparticles composed of atoms from both the target and the liquid medium are created and suspended in the liquid.
- Therefore, ablating the solid target immersed in the liquid by pulsed laser ablation has gained the researcher's attention due to the possibility of producing extreme conditions easily, which in turn leads to forming of new nanoparticles by easily changing the liquid medium and solid target (Zhang *et al.* 2017).

2.5 Nanoparticles-Liquid Reaction

Strong chemical reactions and physical processes will occur among the laser-ablated metal species in the aqueous solution, such as the reaction between water molecules and the ablated species (as charge-transfer interaction and electrostatic forces), because the ablated active species are electronically excited and thus highly reactive, inducing the formation of nanoparticles in solution. Nanoparticles, depending on their size and form, will exhibit different properties in different mediums (Bajaj and Soni 2009). Therefore, solution composition can be utilized to govern nanoparticle properties, while surface modification via surfactant coverage and laser parameter manipulation ought to be able to manage the impact of such aqueous oxidation. Thus, metal oxide metal composite nanoparticles (NPs) can be made through rapid reactive quenching with a surfactant aqueous solution (He *et al.* 2008, Zeng *et al.* 2005).

2.6 Nanotechnology

The The word "nano" originates from the Greek word for "dwarf," and it is used to describe objects that are on the order of a billion (10^9) nm in size. The term "nanotechnology" refers to the development and application of tools, machinery, and equipment that operate on the nanoscale (atomic/molecular) scale, exploiting the peculiarities of materials and devices at this size. Nanoscale materials exhibit physical, chemical, and biological characteristics that are absent in the bulk form of the same materials (Khanna 2016). The electronic and optical industries, as well as the healthcare and agricultural sectors, can all benefit from using nanomaterials. The development of new methods and instruments for the synthesis, characterization, and manipulation of nanomaterials has led to explosive growth in the field of nanotechnology over the past two decades. Nanoscale materials can be produced through a wide range of traditional physical, chemical, biological, and other hybrid processes (Filipponi and Sutherland 2013).

2.7 Nanostructures

Nanostructure is defined as an object having at least one dimension within 1-100 nm. To describe the structures of nanoparticles, it is necessary to distinguish between the number of Nano-dimensions.

According to the dimensionality, the following categories are known:

- Quantization occurs in all three spatial dimensions (1D) in a quantum dot (also dubbed a "quantum box") (Wei *et al.* 2009).
- In a 2D structure, such as a quantum wire, free motion is possible in only one direction because quantization occurs in both directions.
- Particle motion is quantized in one dimension of a two-dimensional (2D) structure or quantum well, yet the particle is free to travel in the other two dimensions.
- The particle's motion is not quantized in a 3D structure or a bulk structure, therefore the particle is at liberty to move in either.

The type of nanostructure and density of states are shown in Figure 2.8 (Narayanan Pradeep 2021).

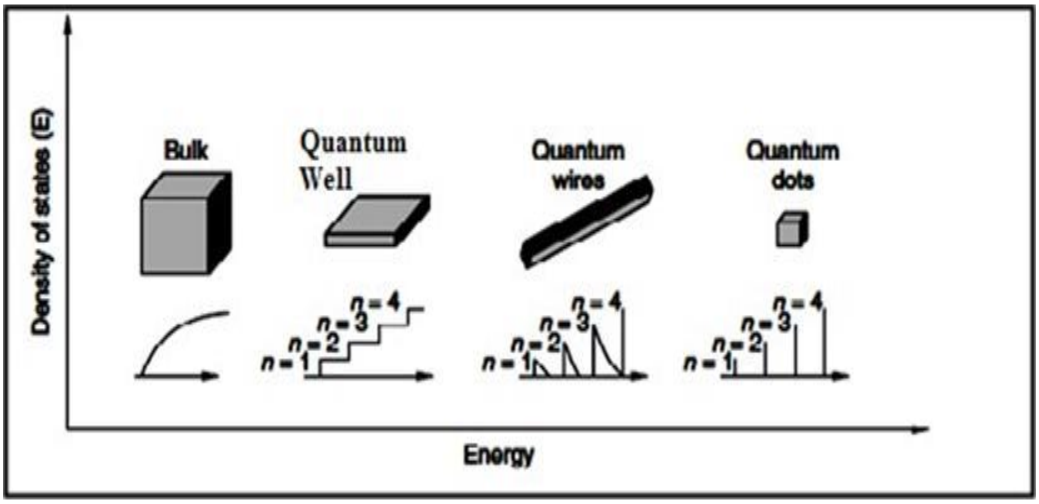

Figure 2.8 Electronic density states and quantum confined systems as a function of the dimension

2.8 Germanium (Ge)

2.8.1 Germanium metal

Germanium (Ge), a chemical element, is represented by the symbol Ge and atomic number 32. Germanium is a glossy, hard-brittle, grayish-white metalloid that is part of the carbon family. Silicon and tin are chemical neighbors in the same group. Pure germanium is an indirect semiconductor that resembles elemental silicon in appearance. In nature, germanium also naturally interacts and forms compound with oxygen (Melcher and Buchholz 2014).

Due to its rarity, germanium wasn't discovered by chemists until fairly recently. Germanium is around the fifty-first most abundant element in the Earth's crust. Dmitry Mendeleev placed Eka silicon on his periodic table in 1869 because he expected the element to exist. Over two decades later, in 1886, Clemens Winkler found the new element, together with sulphur and silver, in the peculiar mineral argyrodite. Mendeleev's expectations for a silicon relative were validated by combining ratios in compounds, despite the new element's resemblance to antimony and arsenic. Winkler named the element after his home country of Germany. In addition to sphalerite, the principal ore of zinc, commercial extraction of germanium currently also occurs in silver, lead, and copper ores (Froelich and Andreae 1981, Melcher and Buchholz 2014).

Germanium is used as a semiconductor in transistors and other electronic devices. The first decade of semiconductor devices were made entirely of germanium. These days, LEDs are mostly used in light bulbs, solar cell applications, infrared optics, and fiber-optic systems. More recently, germanium compounds have been used to make nanowires and as polymerization catalysts. In organometallic chemistry, tetraethylgermanium is one of several useful organ germanium compounds that can be produced using this element. Germanium is widely recognized as an essential part of modern technology (Avarmaa *et al.* 2019).

Germanium is not thought to be essential for any known kind of life. There are a few complex organic germanium compounds being studied as possible medications, but so yet, no results have been encouraging. Because natural germanium compounds are often insoluble in water, similar to silicon and aluminum, they have low oral toxicity. Synthetic soluble germanium salts are nephrotoxic, while synthetic germanium compounds that react chemically with halogens and hydrogen are irritants and poisons (Kroening *et al.* 2011).

2.8.2 Germanium nanoparticles

The synthesis, characterization, and development of these fascinating materials have all taken significant steps forward in recent years, opening up new possibilities for their potential practical uses. The effect of quantum confinement in semiconductor NPs on the optical properties of semiconductors is a primary driver of the growing excitement surrounding this area of research. Because of their superior luminescence properties at the nanoscale compared to their bulk forms, fundamental semiconductor NPs like as silicon and germanium are of tremendous interest (Barcikowski *et al.* 2009, Boucherif *et al.* 2013). Si and Ge NPs require additional research due to their size-dependent optical properties. Optical light-emitting devices, integrated flash memory, solar cell technology, and biomedicine are just a few of the many technologically relevant uses for these materials. formed large crystals The semiconducting properties of Si and Ge make them highly desirable for use in microelectronics (Vadavalli *et al.* 2014). The fastest-developing area of nanoscience and nanotechnology requires the integration of optoelectronic devices with microelectronics that demonstrate effective optical properties. Nanocrystals (NCs) made from silicon (Si) and germanium (Ge) are favored for use in optoelectronics because of their bright visible emission (Desnica *et al.* 2006). Optoelectronics research for optical lighting and display applications can benefit from the use of Si and Ge because they are non-toxic and environmentally friendly green materials that can replace dangerous semiconducting elements. The powerful quantum confinement effects at the nanoscale are responsible for their efficient luminescence at room temperature. In terms of technology, Ge NCs are superior to Si NCs because their Bohr exciton radius is larger (24 nm vs. 6 nm) and their effective masses and energy disparities across the indirect gaps are smaller (Ghosh *et al.* 2013). Synthesizing germanium nanoparticles (NPs) with sizes suited to the required optical and electrical characteristics could prove difficult. Therefore, optimizing new processes for the creation of nanostructures using a wide range of approachable techniques is a vital area of materials research. One relatively fast, affordable, and environmentally acceptable method for creating nanoparticles of the required sizes at room temperature is pulsed laser ablation in liquids (PLAL) from bulk materials (Maeda 1984). Lasers are used for material processing due to their high energy output. Laser ablation is the selective removal of material from a source or bulk target using short laser pulses. When high-intensity pulses are delivered to a material at a controlled pressure and temperature, nanoparticles of the material can be formed in the solution. Laser ablation in liquids has the advantage of being performed at room temperature, and it is possible to manipulate the properties of the nanoparticles by changing the parameters of the liquid and the laser's ablation settings. As a result, this strategy is thought to be effective for developing colloidal nanoparticle solutions. In general, this method of creating nanoparticles is efficient, low-cost, and gentle to the natural world (Maeda 1995, Prabakar *et al.* 2010).

2.8.3 Applications of Ge

In 2007, it was projected that 35% of the world's germanium supply went toward fiber-optics, 30% to infrared optics, 15% to polymerization catalysts, and 15% to electronics and solar electric applications. Phosphors, metalworking, and chemotherapy accounted for the remaining 5% (Geological 2008).

2.8.3.1 Optics

The exceptional index of refraction and low optical dispersion of Germania (GeO_2) have made it a popular material. This allows it to be useful in a variety of imaging applications, including wide-angle camera lenses, microscope objectives, and the core of optical fibers. By replacing titania as the silica fiber's dopant, the brittleness caused by subsequent heat treatment has been eliminated. The United States accounted for less than 10% of the world's yearly germanium consumption in 2002, with most of that going to the fiber optics industry. GeSbTe, a phase change material with excellent optical properties, is used in rewritable DVDs (Rieke 2007).

Since it is transparent at infrared wavelengths, germanium is an important infrared optical material that can be easily shaped into lenses and windows. It is used as the primary optic in thermal imaging cameras for passive thermal imaging and hot-spot identification in military, mobile night vision, and firefighting applications. Infrared spectroscopes and other optical instruments that rely on highly sensitive infrared detectors make use of this technology. Its extraordinarily high refractive index (4.0) need chemical treatment to reduce reflection. In particular, a unique antireflection coating of diamond-like carbon (DLC) with a refractive index of 2.0 creates a diamond-hard surface that can withstand significant environmental stress (Lettington 1998).

2.8.3.2 Electronics

Silicon-germanium alloys can be made by fusing germanium and silicon, which are quickly emerging as key semiconductor components for high-speed integrated circuits. Si-SiGe heterojunctions' advantages allow for substantially quicker circuits than silicon-only designs. In wireless communication devices, silicon-germanium is beginning to take the role of gallium arsenide (GaAs). High-speed SiGe chips may be produced using the silicon chip industry's low-cost, tried-and-true production methods (Geological 2008, Washio 2003).

High-efficiency solar panels are one of the most important uses for germanium. The nearly identical lattice constants of germanium and gallium-arsenide make the latter a viable substrate material for gallium-arsenide solar cells. Germanium is used as a substrate for wafers of high-efficiency multijunction solar cells in space applications like the Mars Exploration Rovers' triple-junction gallium arsenide on germanium cells. High-intensity LEDs have numerous uses, including backlighting LCD displays and lighting automobile headlights (Crisp *et al.* 2004, Geological 2008).

Germanium-on-insulator (GeOI) substrates are being considered as a possible alternative to silicon in miniaturized circuits. Recent research has revealed a CMOS circuit that operates on a GeOI substrate. There are other electronic applications for the phosphors used in compact fluorescent lamps and solid-state light-emitting diodes (LEDs). Several effects pedals, including the Dallas Arbiter Fuzz Face, still use germanium transistors, allowing musicians to replicate the distinctive "fuzz"-tone of the early rock and roll era (Szweda 2005).

2.8.3.3 Other applications

In addition, polyethylene terephthalate (PET) production uses germanium dioxide in polymerization catalysts. The high luminosity of this polyester makes it a popular choice for PET bottles in the Japanese market. In the United States, germanium is not used in polymerization catalysts. Germanium dioxide (GeO_2) is chemically similar to Silicon dioxide (SiO2) and can replace silica as the stationary phase in some types of gas chromatography columns (Fang *et al.* 2007, Geological 2008).

Germanium's application in alloys with precious metals has grown recently. For instance, in sterling silver alloys, it reduces fire scale, improves tarnish resistance, and magnifies precipitation hardening. Patented Argentium silver alloy contains germanium at a 1.2% concentration (Geological 2008).

Semiconductor detectors made from single crystal high-purity germanium may accurately identify radiation sources, for example at airport security. Monochromators made of germanium are utilized in single-crystal neutron scattering and synchrotron X-ray diffraction. In applications involving neutrons and high-energy X-rays, reflectivity is preferable over silicon. In gamma spectroscopy and dark matter detectors, high-purity germanium crystals are employed. Phosphorus, chlorine, and sulfur measurements in X-ray spectrometers are also made using germanium crystals (Bertin 2012, Diehl *et al.* 2006).

Emerging germanium is an essential part of spintronics and spin-based quantum computer infrastructure. Researchers demonstrated spin transport at ambient temperature in 2010, and more recently they discovered that germanium donor electron spins have extraordinarily long coherence periods (Shen *et al.* 2010).

2.9 Gas Sensors

Since the nineteenth century, gas sensors have found widespread application in a wide range of everyday devices. Carbon monoxide (CO) and methane (CH4) sensors have historically been used in hazardous environments like mines to alert workers to the presence of these gases. At the time, the canary was the go-to for spotting gas leaks. Different gas sensing systems have been proposed and implemented to varying degrees over time. The amount of torch, like Flam safety lamps, was a rough indicator of concentration (Ozdemir 2011). The resistance of a wire was measured by burning flammable gas in the first catalytic sensors. Since oxidation and reduction processes take place when exposed to the gas, the amount of gas is measured by the current between two electrodes in electrochemical detecting devices (Röck *et al.* 2008).

The most important field of application of gas sensor devices today is their use in the automotive sector and industry to protect the environment. The detection of nitrogen oxides, CO, CO_2, SO_2, O_2, and H_2 is the main environmental protection concern. And that the different types of sensitivity methods, such as infrared detectors, ultraviolet spectroscopy, or mass spectroscopy, are very reliable and critical methods of even detecting a part per billion (part per billion). These techniques are effective, yet they are too cumbersome, expensive, or difficult to utilize in everyday life to be widely adopted by businesses. However, semiconductor sensor devices excel in cost-effective and portable uses (Franke *et al.* 2006).

When exposed to gaseous species or molecules, gas sensors alter one or more of their physical features. The shift causes an electrical signal, the strength of which is proportional to the number of gas molecules present (Eranna 2011). In addition to its obvious importance in the chemical and petrochemical industries, environmental, scientific, and engineering research, hospitals, and the beverage and food industries also make heavy use of gas sensors (Korotčenkov, 2013). There are four characteristics that form the basis of a sensor's performance: sensitivity, selectivity, reaction time, and recovery time. It is determined by the gas's molecular size and the structure of the sensing layer, both of which are affected by the gas's surface response and diffusion. Catalytic activity of the sensing layer and the working temperature both impact the surface reaction (Yunusa *et al.* 2014). A gas sensor should have these two essential capabilities:

2.9.1 Fundamental parameter of gas sensor

There are several basic parameters that a gas sensor is characterized by.

Sensitivity: Measured as the ratio between the membrane's surface resistance in air (Ra) and the sensor's resistance in the presence of the test gas (Rg), sensitivity is one of the most important sensor parameters. It is determined by invoking the relationship as in Equation (2.1) (Hasan *et al.* 2016).

$$S = \frac{Rgas\ \Omega - R_{air}\ \Omega}{R_{gas}\ \Omega} \times 100\% \quad (2.1)$$

Membrane porosity, thickness, operating temperature, additive presence, and crystal size are only a few of the fundamentals that affect sensitivity (Shimizu and Egashira 1999).

Selectivity: This trait relates to the sensor's capacity to discriminate between different gas mixtures, such as ethanol and methane. when the determination of gas depends heavily on selectivity (Mandayo *et al.* 2003)

Stability: It is a feature that considers repeated measurements of the device following extended use. And that if the performance of the sensor is not demonstrated to be repeatable and reliable, the success of the sensor will be constrained (Park and Akbar 2003).

Time to detection: How long it takes for the gas to cause a 10% increase in sensor output after it has been applied (Hasan *et al.* 2016).

This quality is associated with the sensor's capacity to differentiate between gases that are mixed, such as ethanol and methane. In cases where gas composition is heavily influenced by selectivity (Mandayo *et al.* 2003).

Time of response: When the sensor is exposed to the full gas concentration, as shown in Figure 2.9, the response time is the amount of time it takes for the resistance to reach a predetermined percentage (often 90%) of the final value. Crystal size, additives, electrode geometry, location, and diffusion rates are just some of the sensor parameters that affect response time. The better the sensor, the faster it can react to changes in the environment

(Patel *et al.* 2019). The value of the response time can be calculated through the relationship as in Equation (2.2) (Mays 2016):

$$Response\ time\ =\ |\ tgas(on) - tgas(off)|\times\ 90\% \qquad (2.2)$$

Time of recovery: The time at which the sensor's resistance drops to 10% of its saturation value. The shorter the relaxation time, the better the sensor will be, so that the sensor can be used repeatedly (Patel *et al.* 2019). It can be calculated according to the Equation (2.3) relationship (Mays 2016).

$$\text{Recovery time } =|\text{ tgas (off)} - \text{tgas (recover) }|\times 90\% \qquad (2.3)$$

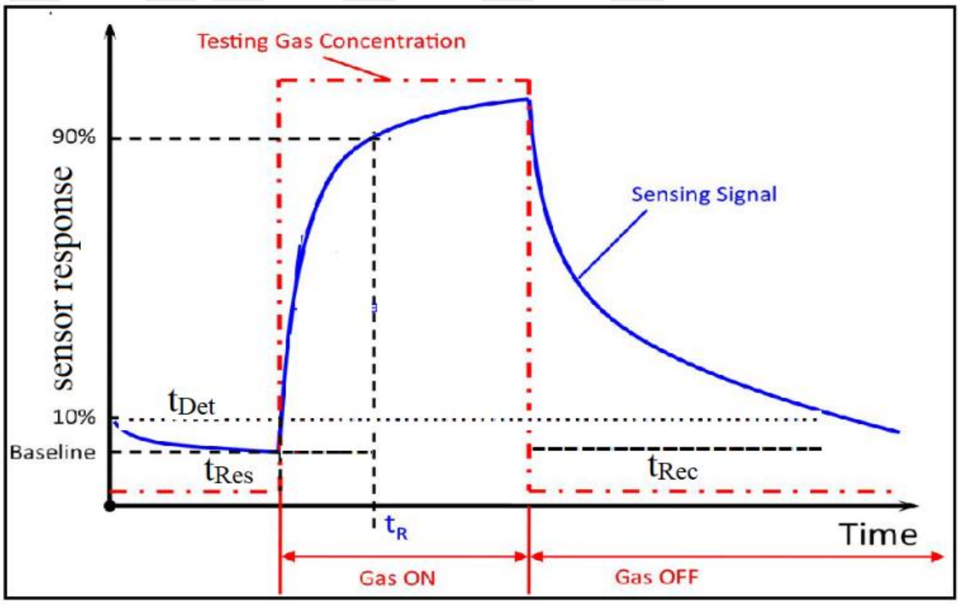

Figure 2.9 Response time and relaxation time (Chen 2010)

2.10 Response Mechanism

Most semiconductor gas sensor systems detect variations in the conduction band electron count as a result of gas-solid interaction, as well as the impact of this (measurable) reaction on the semiconductor's resistance. Local energy levels in the prohibited gap area are made possible since the surface is where the crystal periodic breaks off. Surface states are the energy levels that are accessible at the surface (Barrett *et al.* 1973). These states can absorb or emit electrons, which may come from surface flaws or impurity atoms that serve as electron traps. The Fermi energy of the surface is reduced, and the electronic energy is increased as electrons from the donor plane are drawn to the low-energy surface states in the beam gap. Since the Fermi energy must be the same everywhere in the material when it is in a state of equilibrium, the accumulation of surface charge causes the valence and conduction beams to deflect at the surface (Barsan and Weimar 2001).

As can be seen in Figure 2.10, the donor electrons travel to the surface to aid in oxygen adsorption. On one side of the resulting area, the donor atoms are positively charged, while on the other, the surface states are negatively charged. This region is a depletion zone where charges are lost, and its thickness is indicated by (a). The bending depth is lengthened or shortened depending on the surface charge (Ozdemir 2011).

Some gases interact with species ordinarily absorbed at the sensor layer's pristine surface and are therefore difficult to absorb. Gases with redox properties (or granules) will alter the surface charge density close to the membrane's surface. Exposure of a surface to a reducing gas (such as carbon monoxide) results in the release of electrons, as shown in figure, because the reducing gas interacts with the surface's unabsorbed oxygen. However, an oxidizing gas (such as NO_2) increases the thickness of the depletion layer because its high electronegativity pulls more free conduction electrons from the surface. It has been hypothesized that the effects of moisture changes can be mitigated and oxygen vacancies created by operating at higher temperatures (Ozdemir 2011).

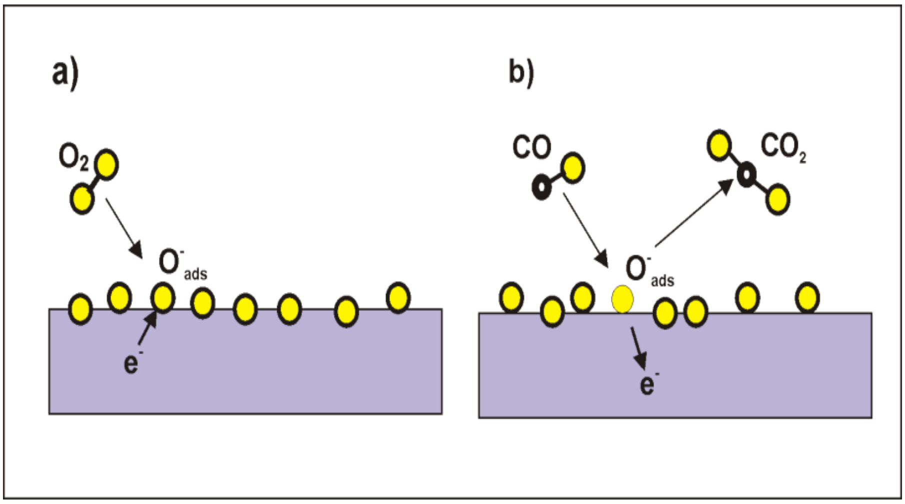

Figure 2.10 (a) The n-type semiconductor membrane undergoes gas-phase oxygen adsorption (b) The electrons are returned to the membrane after oxygen is removed via the reducing gas reaction (CO) (Ozdemir 2011)

3. MATERIALS AND METHODS

In this study, we measured a few things to learn more about the structure, morphology, and optical properties of Ge NPs:

3.1 Diffraction of X-rays (XRD)

In the early days of material science, X-ray diffraction was used to gain insight into solids' internal architecture. Certain frequencies of electromagnetic radiation are bent. Nonetheless, when brought together, they cause both bright and dark areas on the film, known as positive and negative interference, respectively. It is possible to determine the values of network parameters (unit cell dimensions) by carefully analyzing the diffraction patterns. A schematic of the crystal-level Bragg's law and X-ray diffraction is shown in Figure 3.1. The electromagnetic waves known as X-rays have a particular wavelength in the range of (0.1-100) nm, relatively high energy, and are located between gamma and ultraviolet rays (Lehn 1993).

XRD is a vigorous technique utilized because of finding out the crystal structure of crystalline material by means of a diffraction test sample or for measuring the structural properties (strain state, grain size, and distinguish orientation) of its phases, and its non-damaging and doesn't need any elaboration setup. There is a correlation between particle size and the width of the diffraction line; when particles are made smaller, the line widens because their long-range arrangement deviates from that of the crystal. Particle size is calculated with XRD using the Deby Sherrer method as in Equation (3.1) (Zhang 2009):

$$D = \frac{0.9\lambda}{\beta \cos\theta} \tag{3.1}$$

In Equation (3.1), D represents the diameter of the nanocrystal, λ is the wavelength of the light, β is the radian value of the full width at half maximum (FWHM), and the Bragg angle θ.

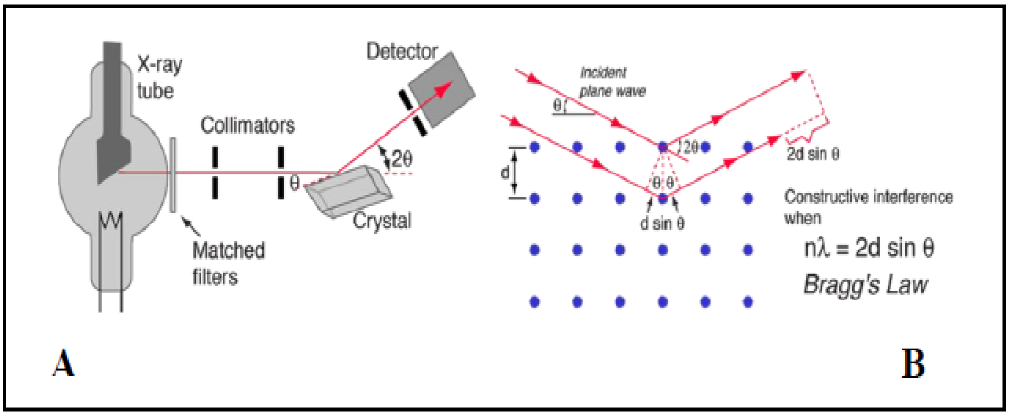

Figure 3.1 Diffraction by X-rays. crystal structure, Bragg's law, and the X-ray diffraction pattern are shown below (Lehn 1993)

3.2 Electron Microscopy Scanning

Scanning electron microscopy (SEM) is an electron microscopy technique used to confirm nanomaterials' performance characteristics. The SEM technique is distinguished by its high magnification (more than one million times) and high resolution (a few nanometers). This testing strategy is easy to implement and modify. The SEM technique reveals information about the surface topography and composition. This is indicated by the way in which the electron beam interacts with the surface of the specimen (Goldstein *et al.* 2017).

3.3 UV-Visible Spectroscopy

Electronic level changes between atoms or molecules are the focus of ultraviolet-visible spectroscopy. Depending on the particle's size and shape, the metallic nanoparticles' absorption peaks will have a different color. Earlier in the 20th century, Mie researched and refined the theoretical foundations of established color. He had started working on Maxwell's equations for how metal particles absorb and scatter electromagnetic radiation. The colloidal containing the nanoparticles will absorb the electromagnetic waves, and the nanoparticles' interaction with the electromagnetic field will cause the valence band electrons to vibrate coherently. This surface ensuing resonance is known as plasmon and happens in the same way that nanoparticles do. Therefore, ultraviolet-visible spectroscopy is thought to be an appropriate technique for identifying nanoparticles' optical properties (Link and El-Sayed 1999). The following Equation (3.2) illustrates the quantitative relationship and law (the law of Beer) between the amount of material and the intensity of the passing light when monochromatic light is transmitted through a solution. If the creation of color is proportional to the amount of substance in the solution, then the amount of light absorbed at this wavelength can be used as a concentration indicator:

$$I_T = I_O \exp - \propto t \tag{3.2}$$

where:

- $I_\circ$: The intensity; of light passing; through the pure; solution.
- I: The intensity; of light when; adding color; compound.
- α: Absorption coefficient
- t: Thickness

The process and components for creating Ge NPs using pulsed laser ablation are detailed in this chapter. It also includes equipment for analyzing the nanoparticles' characteristics after they have been produced (Figure 3.2).

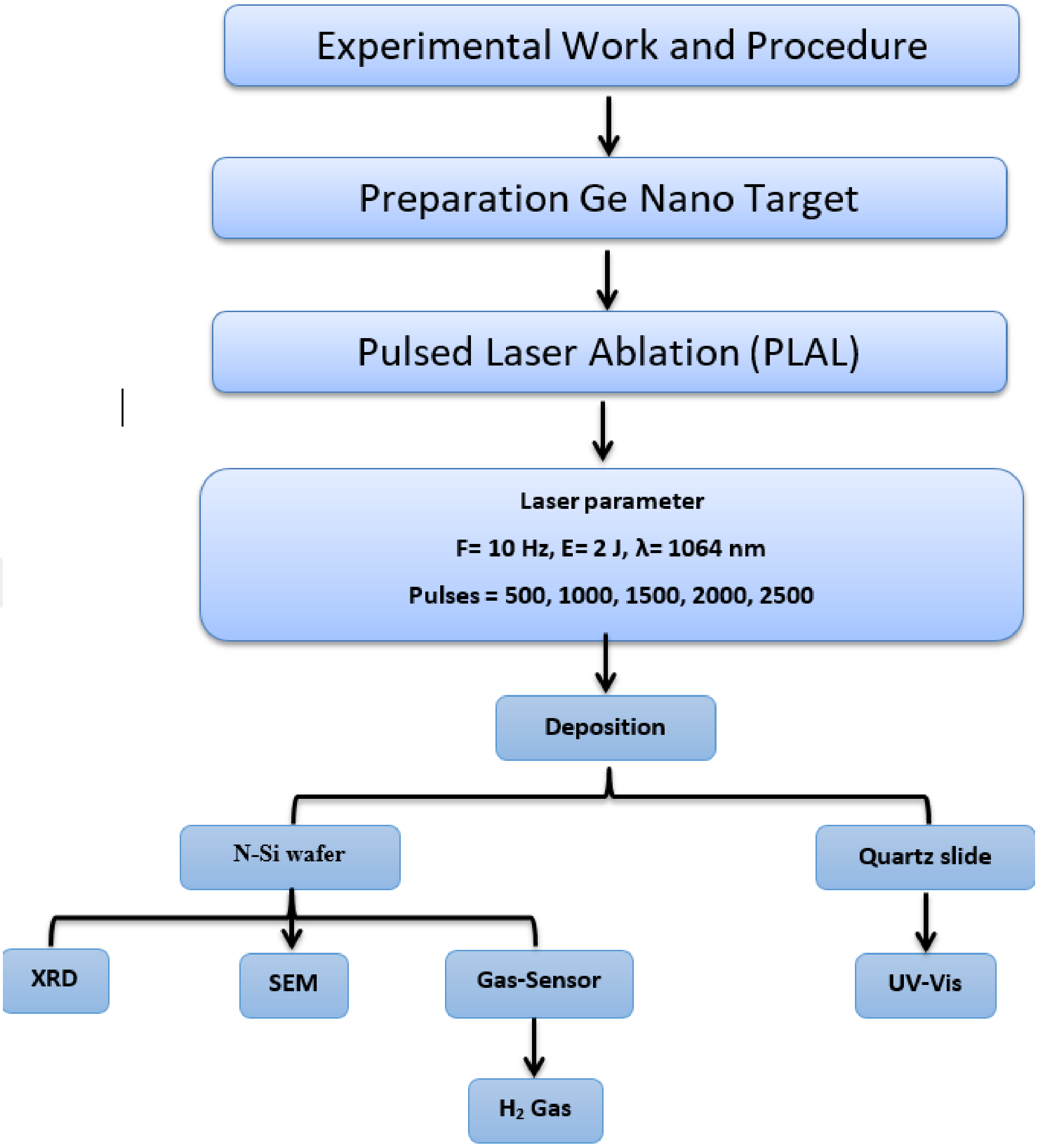

Figure 3.2 The experimental procedure as a flowchart

3.4 Liquid-Based Laser Ablation

Figure 3.3 depicts a practical use of the pulsed laser ablation in a liquid environment technique. Pulsed laser ablation of a Ge target positioned at the bottom of a glass tank holding 3 mL of deionized water was used to create the nanoparticles. The target was exposed to Nd: YAG lasers with 2J of energy, 10 Hz of repetition rate, and 500, 1000, 1500, 2000, and 2500 ms of pulse duration. To ensure that the nanoparticles didn't act as a shield against the laser radiation reaching the target surface, the vessel was rotated while it was being irradiated.

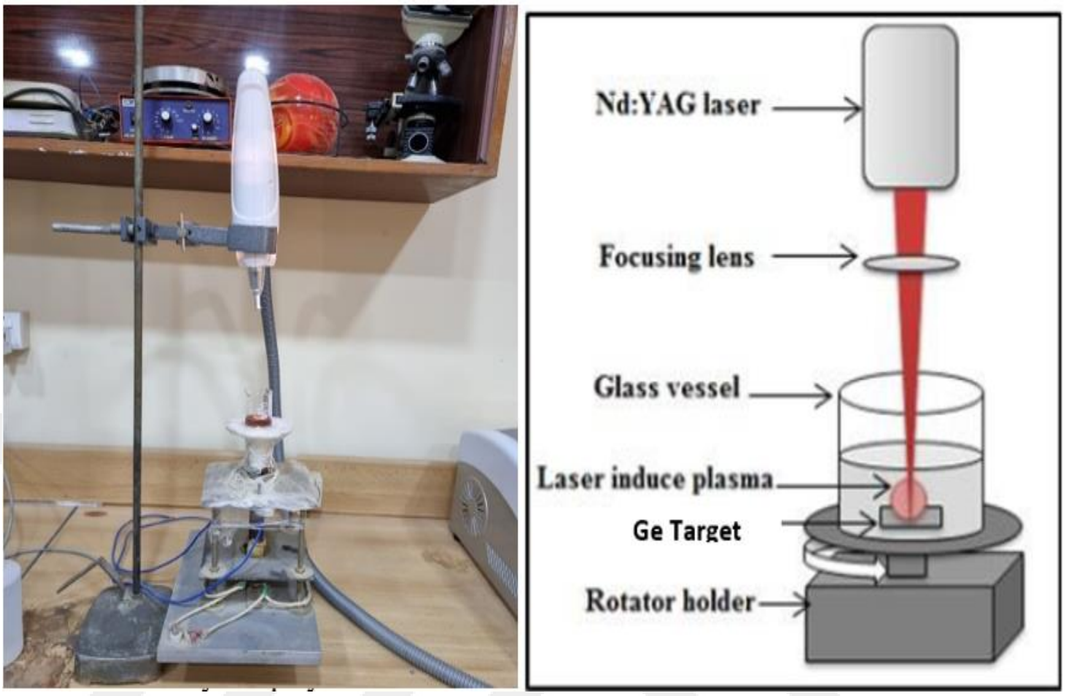

Figure 3.3 Laser ablation in liquid Ge Nps

3.4.1 The source of laser

Ablation was performed using a pulsed Nd: YAG laser system (HUAFEI), providing the pulses with a fundamental infrared wavelength of 1064 nm. The active medium in this laser is Nd: YAG crystal, which operates in Q- switched mode, the output length of the pulse is (10) Hz. The energy used was 2J Laser pulse energy (Genetic QE 12SP-SMT) obtained by the play meter after calibration. Laser numbers of shots range from 500 to 2500 pulses.

3.4.2 Cell holder

The rotation speed of the cell holder was (5 rpm) and provides the following features.

- Get uniform removal for the following pulses to ensure identical irradiation conditions during laser exposure.
- Laser pulses can cause extensive ablation and crater development on the target surface, thus it's important to avoid tracing them.

3.5 Chemical Thermal Spraying

A thermal chemical spraying technique was adopted in the preparation of the thin films used as a gas-gas sensor. The figure 3.4 shows the thermochemical decomposition system, which consists of the following parts:

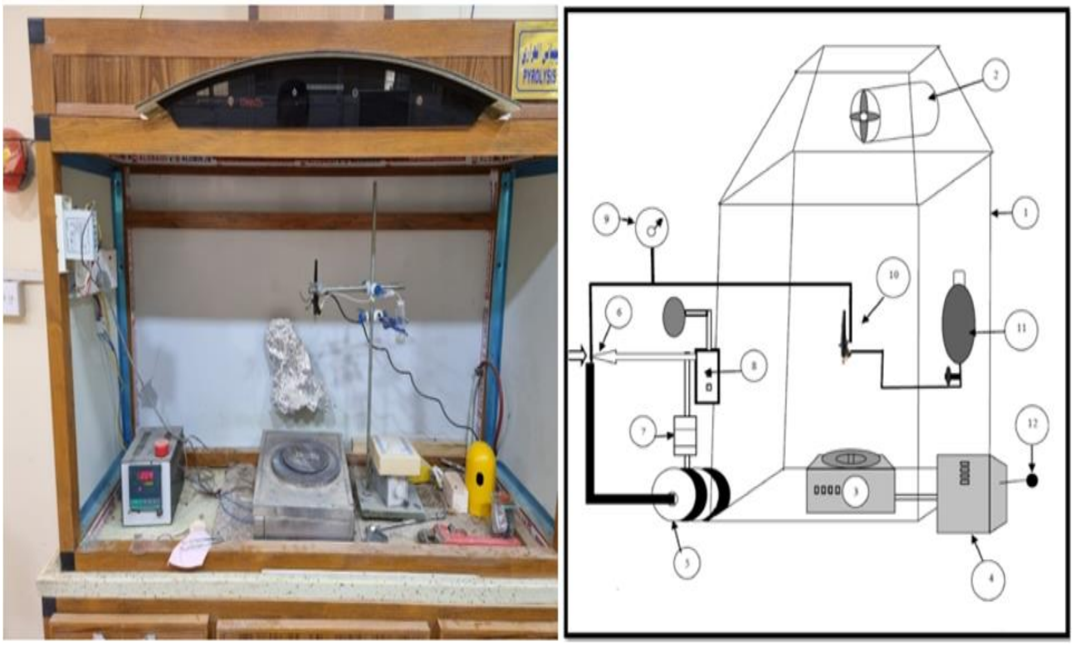

Figure 3.4 Thermal chemical spray system

1. the air, 2. air puller, 3. electric heater, 4. digital thermostat, 5. air pump, 6. air valve, 7. running counter, 8. on a timer, 9. pressure gauge, 10. Spray device, 11. solution container and 2. ac power supply

3.6 Substrate Preparation

3.6.1 Quartz substrate

Microscope slides, made of China national machinery, have been used with a thickness of 1.2 mm, with dimensions of 25.4 x 76.2 mm^2. The process of cleaning the bases is an important stage because it greatly affects the quality of the prepared films and the accuracy of their examination, so the process of cleaning the bases goes through several stages after they are cut into pieces with dimensions ranging about (1.5 x 1.5 cm^2) where they are washed using ordinary water and liquid soap, then it is cleaned by submerging it in distilled water in a glass container, which is then placed in an ultrasonic bath's water basin for 15 minutes, and finally, it is submerged in methanol alcohol in another glass container for the purpose of sedimentation.

3.6.2 Silicone substrate

We used n-type silicon precipitation bases, which were cut into pieces about (1.5 x 1.5 cm^2) in size before being cleaned in a plastic container with hydrofluoric acid (HF) diluted with distilled water by volume (1:10), rinsed in distilled water and alcohol, patted dry with tissues, and then placed in a separate container designed for sedimentation.

3.7 Prepare Germanium Nanoparticles

Figure 3.5 depicts the experimental setup utilized during the laser ablation approach used to create liquid medium suspensions of Ge NPs.

The pulsed laser ablation in a liquid environment experiment is depicted in Figure 3.5. Pulsed laser ablation of Ge was used to create the nanoparticles, and the Ge target was submerged in 3 ml of Non-Ionic Water in a glass beaker. Nd: YAG was used to irradiate the target. The HUAFEI laser system was employed for the ablation, and its fundamental infrared laser pulses had a wavelength of 1064 nm. This laser uses Nd: YAG crystal as its active medium; it generates its light in a Q-switched mode; and its output pulses have a 10-hertz frequency. Exactly 2000 mJ of energy was expended. After calibration, a game meter was used to determine the laser pulse energy (Genetic QE 12SP-SMT) at 500, 1000, 1500, 2000, and 2500 pulses.

The cell holder rotates at (5 rpm) and offers the following features:

- Get uniform removal for the following pulses to ensure identical irradiation conditions during laser exposure.
- Repetition of laser pulses in the same place can cause deep ablation and cratering on the target surface, which must be avoided.

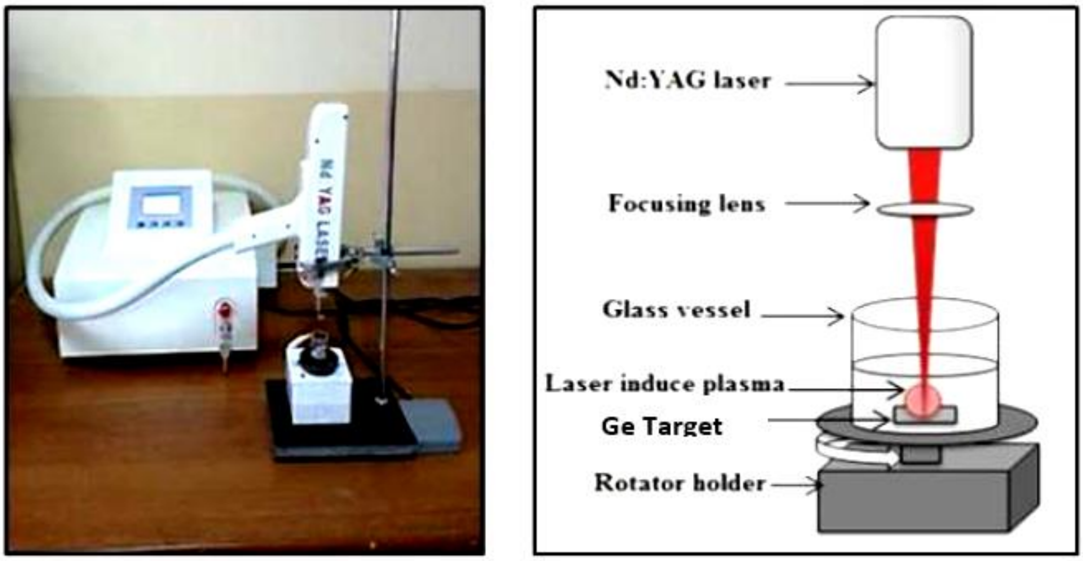

Figure 3.5 Schematic diagram of laser ablation set-up of Ge NPs

3.8 Deposition of Thin Films

To ensure that the surface temperature of the glass bases reaches the required temperature for the deposition process to begin, they are placed on the surface of the electric heater for 10 minutes after they have been cleaned and dried, and after installing the spray device on the metal stand the distance between the end of the spray device and the bases is set to (29 cm), after which the solution of the substance to be deposited is placed in the tank of the spray device. The amount of flowing solution is controlled through a valve in the spray device to reach the required spray rate (2ml/min), then the gas valve is turned on and at the same time, the spray time is adjusted using an electronic timer so that the spray time is 5 seconds, and the stop time is 20 seconds to ensure the return Degree.

3.9 The Measurement Techniques

In this study, we take various measurements to learn more about the structure, morphology, and optical properties of Ge NPs.

3.9.1 Device for X-ray diffraction

Crystalline characteristics are analyzed by studying their X-ray diffraction patterns with a (Philips PW) X-ray diffractometer. In this context, the intensity is reported as a function of the Bragg angle. The parameters for this measurement are as follows. Beam characteristics include wavelength (1.5406 ° A), current (30 mA), and voltage difference (40 kV) from a (Cu-k) source. Additionally, the diffraction angle (2) needs to be in the range of (20-80).

3.9.2 Utilizing SEM (scanning electron microscopy)

The films of varying magnifications and detectors were used in a scanning electron microscope (SEM; manufacturer: HITACHI, Japan) study of the manufactured films' topography. Particle size analysis made use of it as well. SEM's pump down to 10-5 bar will take around 3–4 minutes. The gas panel's EHT (beam voltage) is adjusted to the required value, often between 5 and 20kV. The Islamic Republic of Iran's University of Kashan handles the processing of these exams.

3.9.3 A UV-visible spectrophotometer

The optical absorbance spectra of colloidal Cuo nanoparticles were determined using a UV-Visible spectrophotometer (wavelengths between 200 and 900 nm). The quartz cell contains the samples at varying concentrations and exposure times, and the optical path is 1 cm in length. Difference in energy, spectrum of transmission, and absorption range.

3.9.4 Gas sensor

In order to conduct sensitivity measurements for (Ge) films, it is necessary to deposit aluminum electrodes on these films as shown in Figure 3.6 by using the masks for this examination. These electrodes were obtained by placing a pure aluminum wire inside the tungsten basin. In the vacuum thermal evaporation system, in order to melt it and then evaporate it to settle on the membranes in the system.

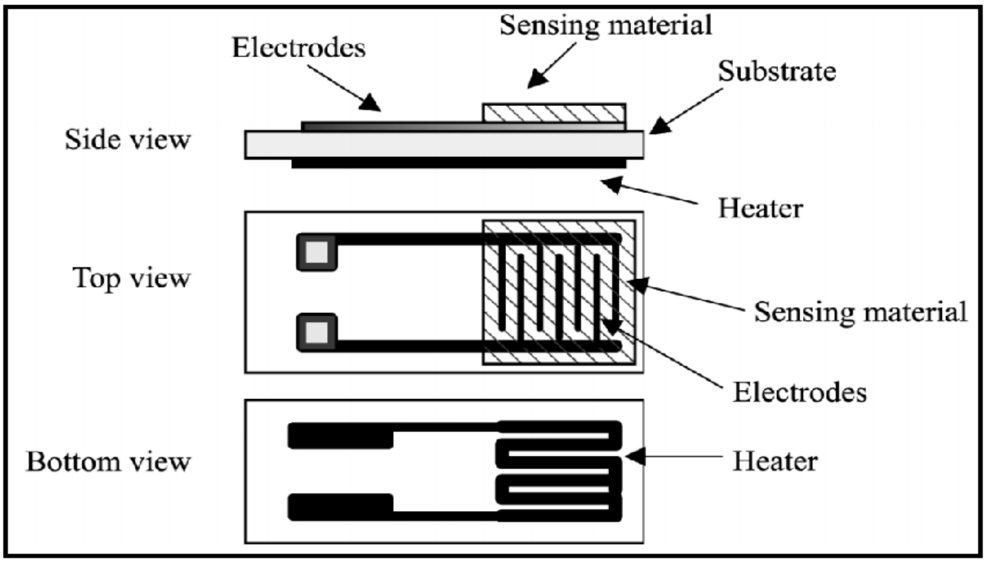

Figure 3.6 Typical gas sensor setup

Figure 3.7 depicts the gas sensor testing setup. a stainless-steel cylinder with a diameter of 30 cm and a height of 35 cm used for conducting tests. The chamber has a valve for admitting the test gas and another for admitting air after the procedure is over. Its actual volume is (6594 cc). At the base of the room, there is a multi-pin clip that allows electrical connections to reach the heater, thermal sensors, and electrodes. A digital multimeter (UNI-T UT81B) connected to a portable computer is used to record the change of the sense current when the gas pressure or temperature is changed. True sensitivity is achieved by feeding the mixture through a tube over the sensor device into the testing chamber.

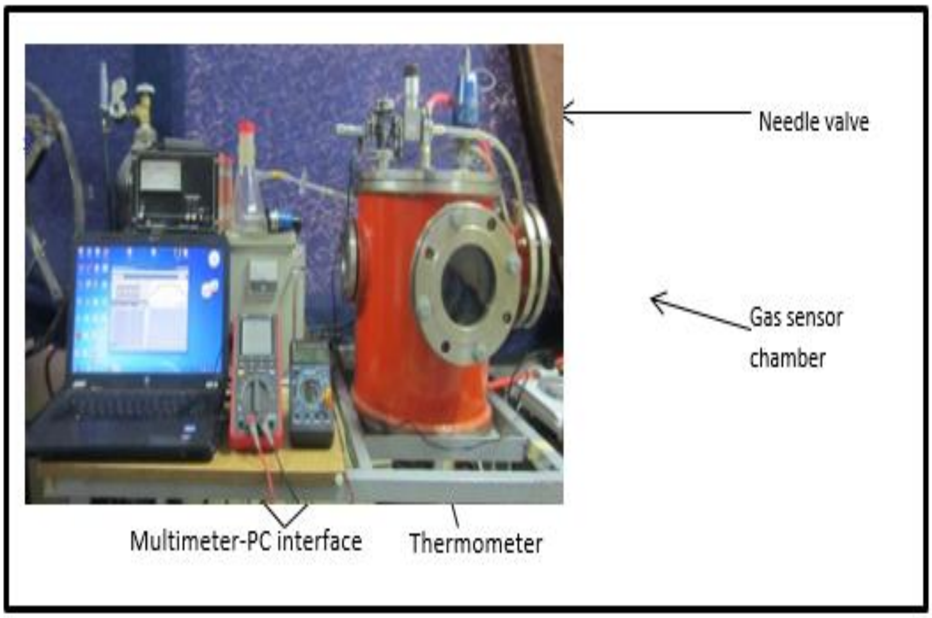

Figure 3.7 Components of the gas sensor

4. RESULTS AND DISCUSSION

In this chapter, we look at the experimental measurements that were taken to determine the optimal number of pulses for creating germanium nanoparticles by PLAL. Ge NPs produced on a silicon substrate via thermal chemical spraying have been analyzed for their structural and optical properties. The constructed (Ge) membranes' gas sensor capabilities were also investigated in this chapter, with their sensitivity, response time, and relaxation time all being computed.

4.1 The Analysis of X-Ray Diffraction (XRD)

Figure 4.1 shows the X-ray Diffraction (XRD) decoration of the prepared Ge Nanoparticles by using a Pulsed Laser Ablation and laser wavelength 1064nm with energy 2000 mJ with different number pulses (500, 1000, 1500, 2000, 2500) of Germanium (Ge).

Ge NPs were synthesized through the Pulsed Laser Ablation method, whose structural formation was afterwards validated, X-ray diffraction analysis was measured of prepared samples with different number pulses (500, 1000, 1500, 2000, and 2500) at an energy 2000 mJ, as and Laser wavelength 1064 nm, as shown in Figure 4.1. It can be observed that all XRD patterns with different numbers have crystallized very well. there are three diffraction peaks of (2θ= 54.67, 56.44, and 61.80), corresponding to the crystalline planes (202, 210, and 113) these peaks are related to GeO2, these diffractions related to hexagonal structure with (ICSD 98-063-7456), addition, we can observe additional new diffraction peaks related to Ge_2O_4 at (2θ=47.84, 66.63) corresponding to the plane (120, 002), these diffractions are related to Orthorhombic structure with (COD 96-900-6860). diffraction peaks related to Germanium Oxide with structure orthorhombic structure. It has been noted that, except for the example (2500), the strength of all the peaks increases steadily as the number of pulses increases. As can be seen in Figure 4.1, an increase in concentration also led to an increase in particle size, which in turn led to an increase in agglomeration and sedimentation of the manufactured nanoparticles. The value of average crystallite size that shown in Table 4.1, was determined using Scherrer's equation.

Table 4.1 Structural properties of the prepared films

Sample	2θ (Deg.)	FWHM (Deg.)	Crystalline size (nm)	Dhkl (°A) Practical	(hkl)	Phase
500 PLS	54.6508	0.1008	96.4	1.67805	202	GeO_2
	56.4224	0.1344	71.3	1.62949	210	GeO_2
	61.7757	0.1344	68.9	1.50051	113	GeO_2
	66.6867	0.168	59.4	1.40142	002	Ge_2O_4
1000 PLS	47.8467	0.09	106	1.89956	1 2 0	Ge_2O_4
	54.6754	0.09	109.1	1.67736	2 0 2	GeO_2
	56.4453	0.09	100.2	1.62889	2 1 0	GeO_2
	61.8017	0.09	112.9	1.49994	1 1 3	GeO_2
	66.6334	0.1867	53.1	1.40241	0 0 2	Ge_2O_4
1500 PLS	47.8467	0.09	106	1.89956	1 2 0	Ge_2O_4
	54.658	0.1068	90.3	1.67785	2 0 2	GeO_2
	56.4322	0.1432	100.2	1.62923	2 1 0	GeO_2
	61.7867	0.121	68.6	1.50027	1 1 3	GeO_2
2000 PLS	47.8095	0.1413	65.2	1.90095	1 2 0	Ge_2O_4
	54.66	0.1131	85.1	1.67779	2 0 2	GeO_2
	56.4367	0.1036	94.3	1.62911	2 1 0	GeO_2
	61.796	0.1225	80.9	1.50006	1 1 3	GeO_2
	66.6131	0.179	55.6	1.40279	0 0 2	Ge_2O_4
2500 PLS	47.7817	0.2406	37.3	1.90199	1 2 0	Ge_2O_4
	54.6281	0.2406	38.4	1.6787	2 0 2	GeO_2
	56.3694	0.6015	15.2	1.6309	2 1 0	GeO_2
	61.768	0.2887	32.9	1.50068	1 1 3	GeO_2
	66.6264	0.3128	31.2	1.40254	0 0 2	Ge_2O_4

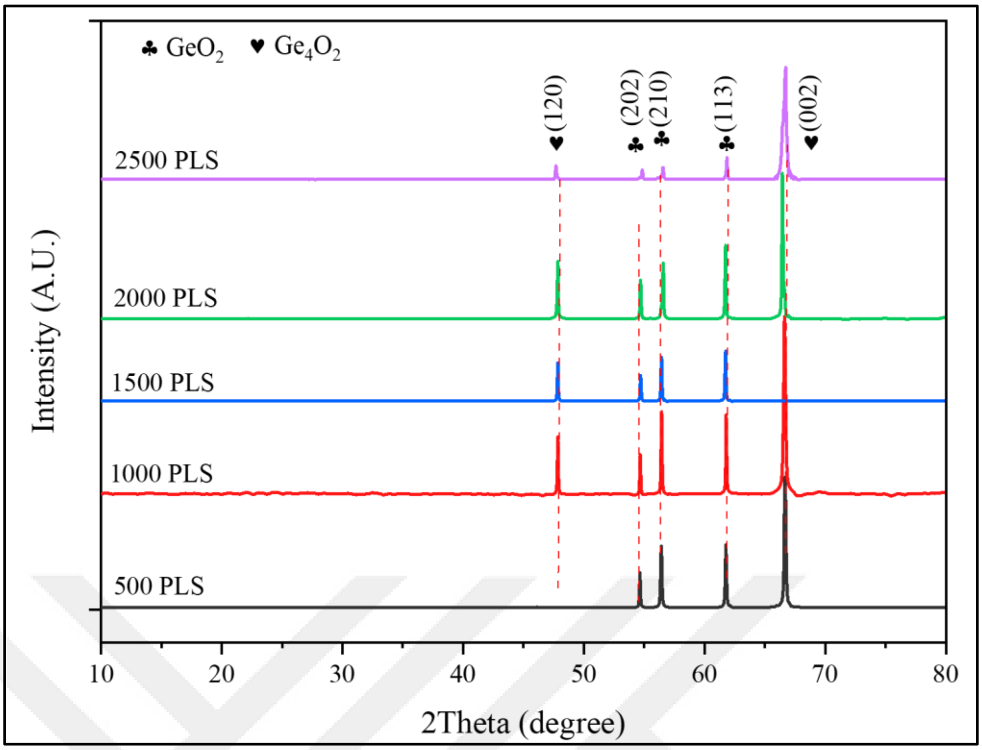

Figure 4.1 XRD pattern of Ge prepared with Pulse number (500, 1000, 1500, 2000, 2500)

4.2 Optical Properties

A material's optical properties include its ability to absorb, reflect, and transmit light. A material's optical characteristics can be determined by observing how it reacts to various colors of light. Some of the optical properties that can be measured include.

4.2.1 Absorption spectra

The UV-vis absorption spectrum from 200 to 1100 nm was used to analyze nanoparticle production. UV-vis absorption spectroscopy was utilized to characterize a Ge solution sample containing various pulses (500, 1000, 1500, 2000, and 2500). Figure 4.2 depicts the UV-vis absorption spectra obtained from these measurements. The absorption spectra have a peak right around 300 nm. The absorption increased with the increase of laser pulse number, there was a low value at 500 pulses and a high value at 2500 pulses. Ablation results in a higher concentration of metal nanoparticles in solution, which can explain the enhanced absorption intensity. It was also found that the intensity of the laser influenced the amplitude and width of the absorption peaks. The creation of germanium nanoparticles is indicated by the absorption peak around 300 nm, with the peak position being nearly constant (Figure 4.2). After numerous pulses of the experiment, the solution took on a discernible hue. The absorbance of a suspension varies with its concentration in accordance with the Beer-Lambert law. However, an increase in concentration can be triggered by an increase in the number of gaps in nanoparticles, leading to diffusion at the Fermi level, and an increase in the number of permitted states, which can be thought of as an energy gap.

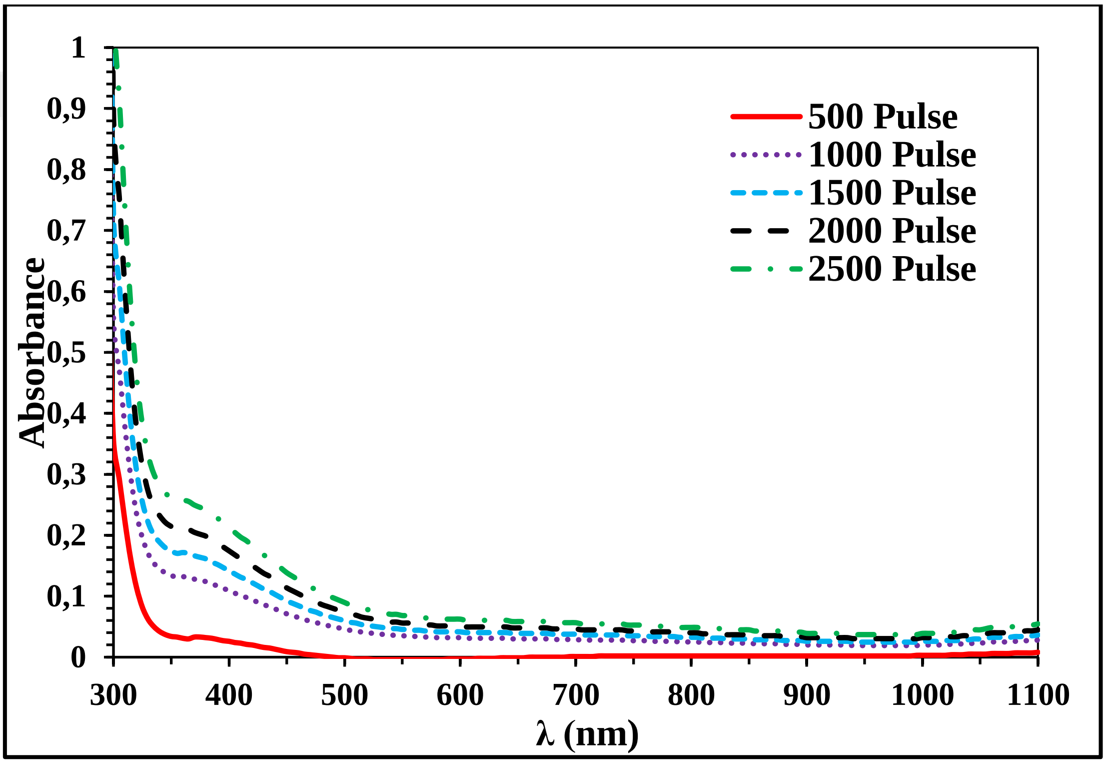

Figure 4.2 Ge nanoparticle absorption spectra for a range of laser pulse intensities (500, 1000, 1500, 2000, 2500)

4.2.2 Optical energy gap

It's how much power is needed to get electrons from the valence band to the conduction band. The strength of the optical energy was calculated and a linear relationship was drawn between $(\alpha hv)^2$ and the energy of the incident photon (hv) and the intersection of the straight tangent with the energy of the photon when $(\alpha hv)^2=0$, we get the optical energy gap at the allowed direct transition, and the measurements of (UV-vis) showed through Figure 4.3, Figure 4.4, Figure 4.5, Figure 4.6 and Figure 4.7, we notice that the values of the energy gap for germanium increase when the number of pulses increases due to the decrease in the crystal size, which is inversely proportional to the energy gap, as the Fermi level shifts towards the conduction level, so the energy gap increases, and this agrees with the researcher (Table 4.2).

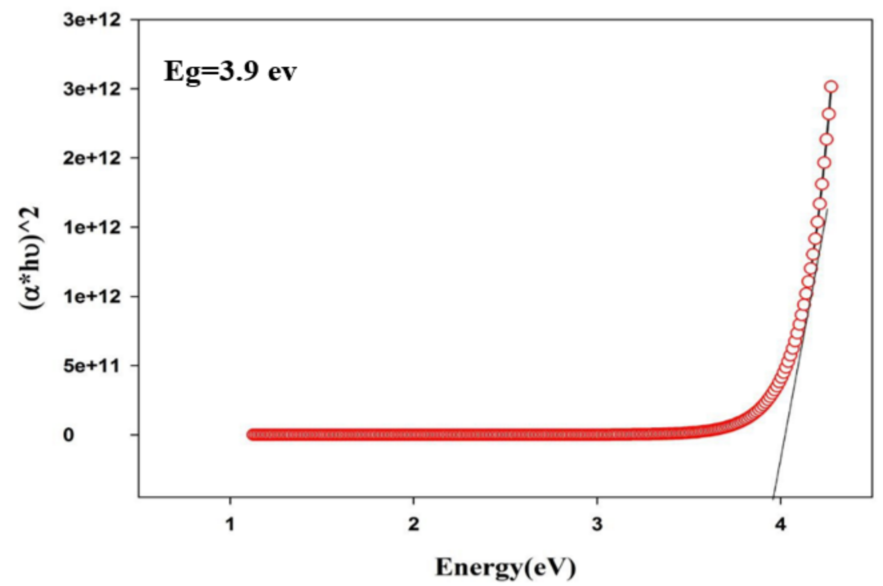

Figure 4.3 The energy gap for Germanium at the number of pulses 500

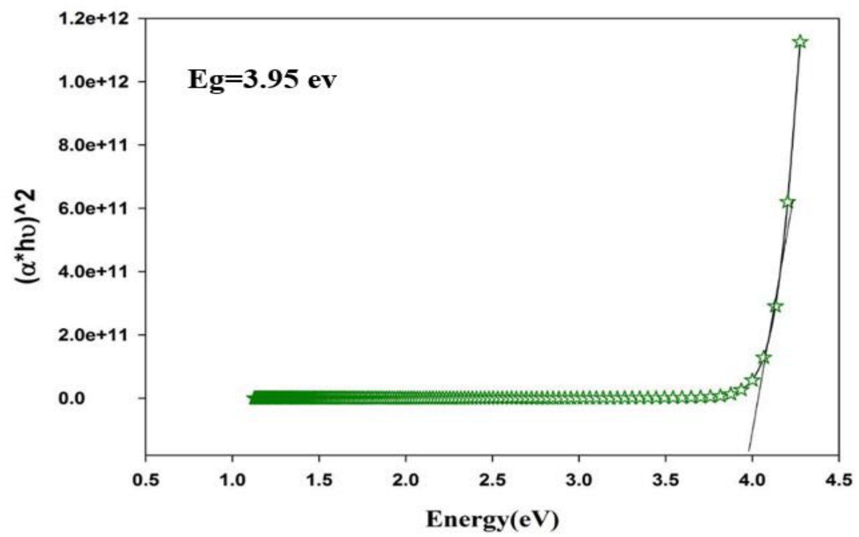

Figure 4.4 The energy gap for Germanium at the number of pulses 1000

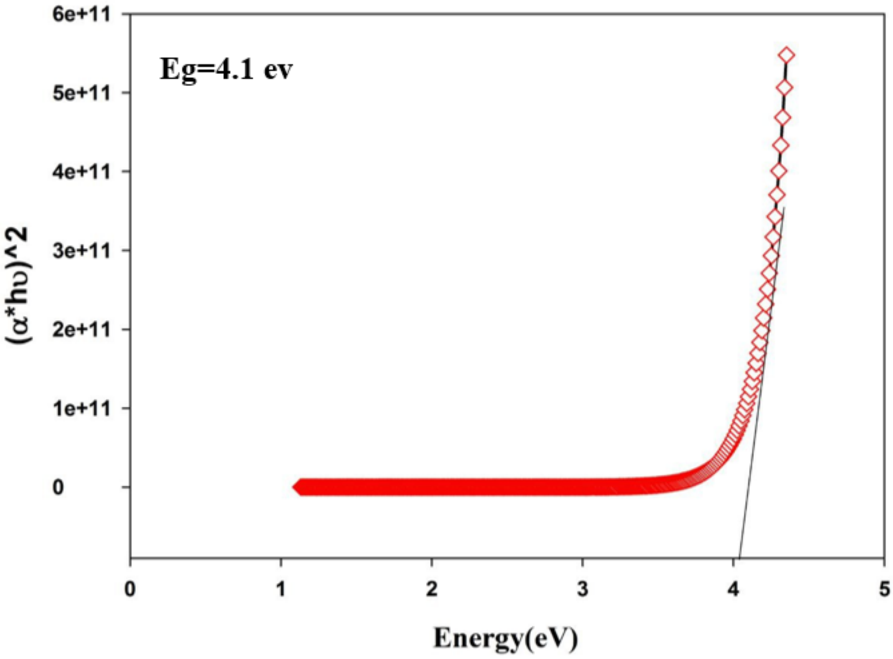

Figure 4.5 The energy gap for Germanium at the number of pulses of 1500

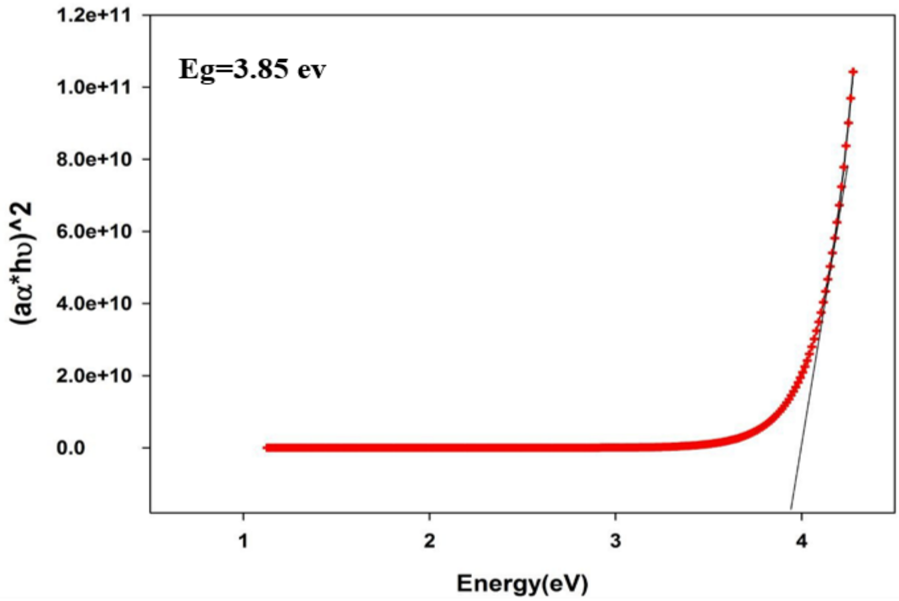

Figure 4.6 The energy gap for Germanium at the number of pulses 2000

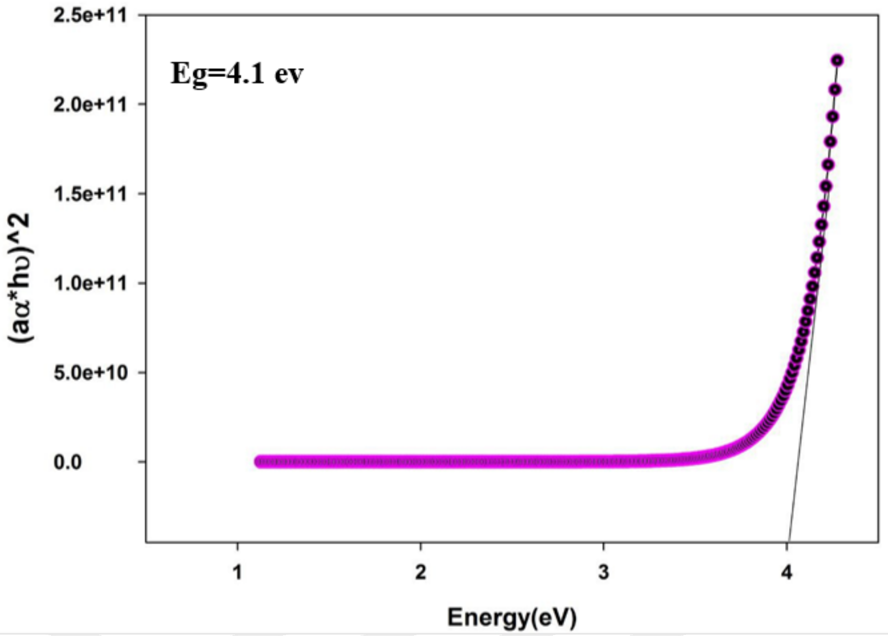

Figure 4.7 The energy gap for Germanium at the number of pulses 2500

Table 4.2 Value of energy gap for germanium at different pulsed laser number

Pulsed NO.	Eg opt (ev)
500	3.9
1000	3.95
1500	4.1
2000	3.85
2500	4.1

4.2.3 Transmittance (T)

The wavelength dependence of the transmittance of germanium nanofilms is plotted in Figure 4.8. Where the maximum value appears at 500 pulses and then decreases with increasing pulses, and this is because the transmittance depends on several factors, including the thickness of the membrane, and is inversely proportional to it, since increasing the thickness allows the occurrence of optical absorption processes and thus slows down a large part of the incident beam on the membrane. The transmittance reduces as the doping concentration rises due to an increase in the number of hits, which increases the number of local levels between the valence and conduction bands

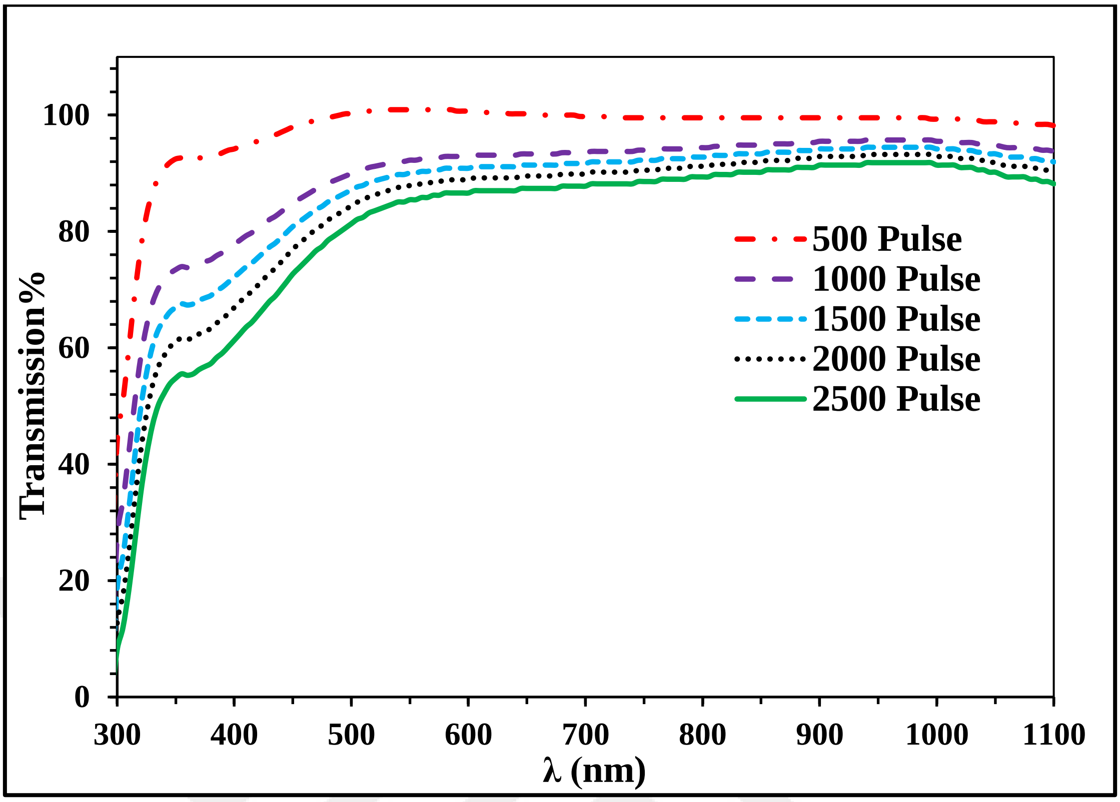

Figure 4.8 The transmittance spectra of Ge nanoparticles with different laser pulse numbers (500, 1000, 1500, 2000, 2500)

4.2.4 The absorbance coefficient

The nanocomposite's absorption coefficient (cm^{-1}) is plotted against wavelength for different pulses numbers in Figure 4.9. Since the energy of the incident photon is insufficient to move electrons from the valence band to the conduction band, the probability of electronic transitions occurring at low energies (at long wavelengths) is very small. At high energies (at short wavelengths), there is a high possibility of electronic transitions because the change in the absorption coefficient is substantial. Therefore, the photon's energy is sufficient to cause the electron to transition from the valence band to the conduction band, and knowledge of the nature of these transitions may be gained from the absorption coefficient.

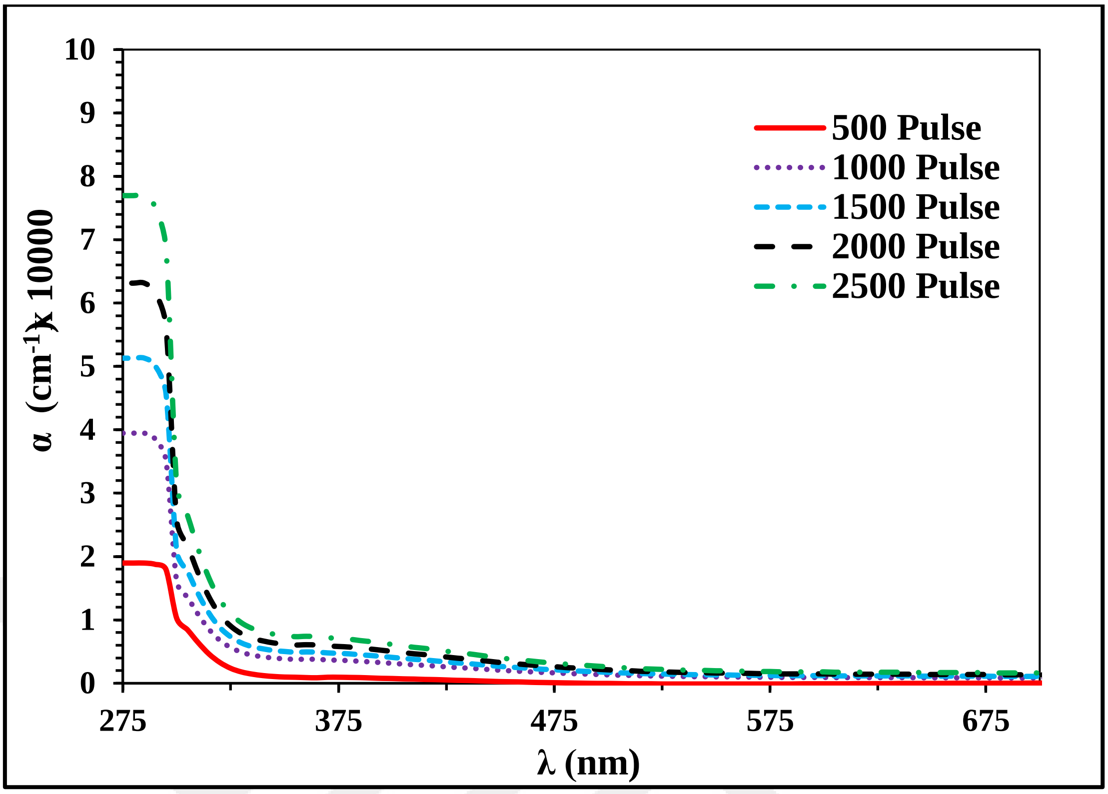

Figure 4.9 The absorbance coefficientof Ge nanoparticles with different laser pulse numbers (500, 1000, 1500, 2000, 2500)

4.2.4.1 Refractive index (n)

It is the relationship between the refractive index (n) and the wavelength (λ) that is shown in Figure 4.10. To increase the density of germanium nanoparticles due to a rise in the number of free electrons. It is noted that the refractive index increases with increasing the number of pulses (raising the concentration) of germanium. High values of the refractive index are observed in the ultraviolet region because of the low transmittance in this region; it is also observed that the refractive index values change with the increase in wavelength, after which the refractive index begins to decrease; furthermore, it is observed that the behavior of the refractive index of the films increases with the increase in the added concentration (increasing the number of pulses)

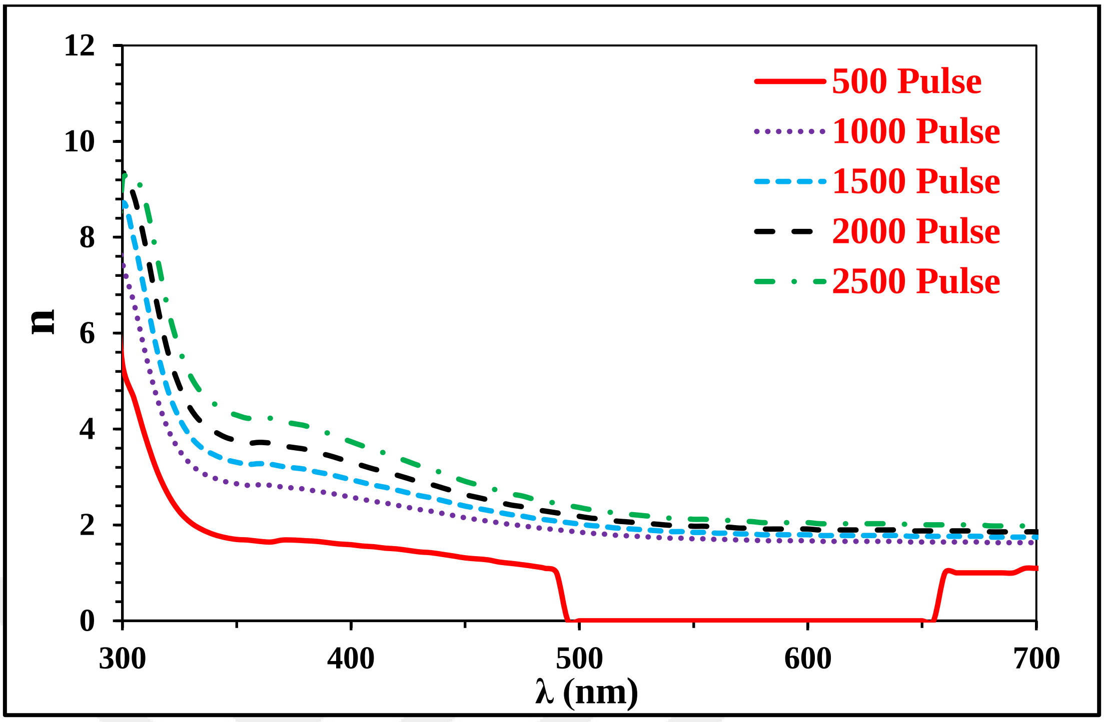

Figure 4.10 The effect of changing the number of laser pulses on the refractive index (n) of Ge nanoparticles (500, 1000, 1500, 2000, 2500)

4.2.5 Coefficient of extinction (k)

The Extinction Coefficient (k) quantifies the degree to which an electromagnetic wave is deactivated or absorbed by a thin film. The complex refractive index has an imaginary part that is represented by this symbol as well. The variation in quenching coefficient between (300) and (800) nm is depicted in Figure 4.11. Loss of incident wave energy owing to the optical absorption process influences the Extinction coefficient in a manner analogous to that of the absorption coefficient. The amount of radiation attenuated via the membrane is directly proportional to the wavelength, hence a smaller Extinction coefficient (k) is observed with longer wavelengths. However, it should be noted that (k) increases with the increase in concentration of the added substance (increasing the number of pulses), so the intensity of the incident beam is attenuated as the energy of the incident rays increases

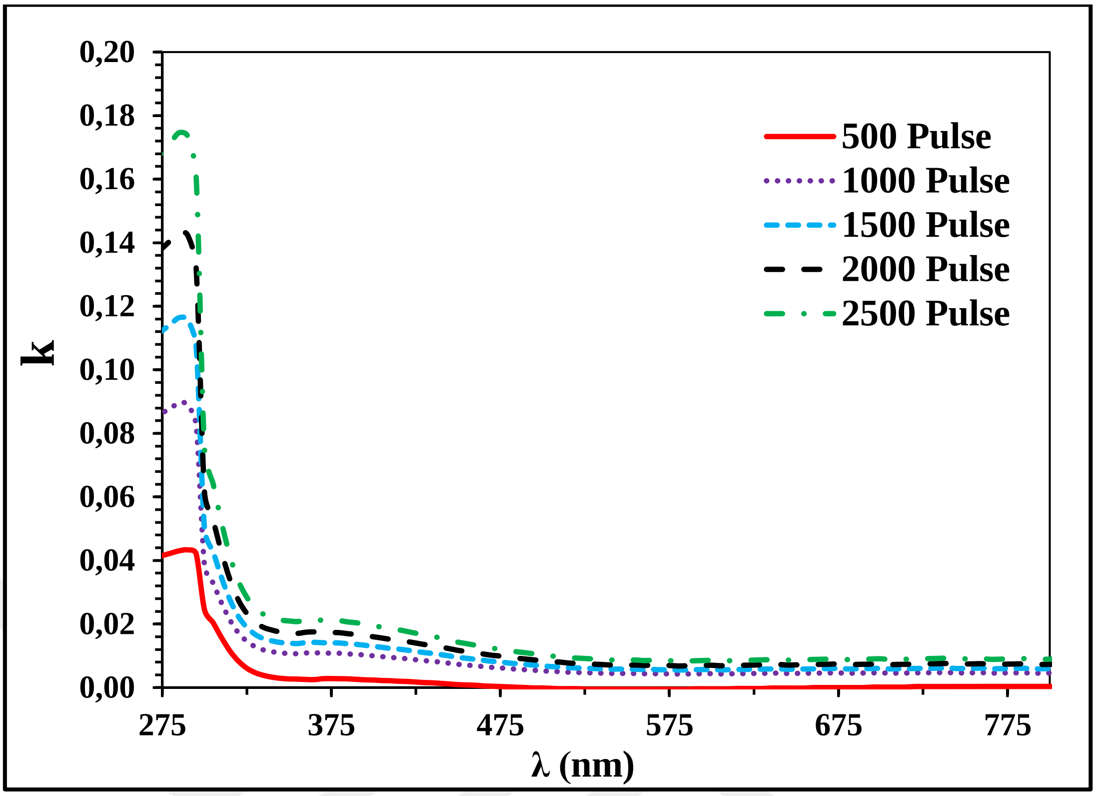

Figure 4.11 Ge nanoparticles' extinction coefficient (k) as a function of laser pulse number (500, 1000, 1500, 2000, 2500)

4.2.6 The real and the imaginary part of dielectric constant (εr, εi)

The Figure 4.12 and Figure 4.13 show the change of the dielectric constant **(εr, εi)** in its real and imaginary parts as a function of wavelength, and it is noted that the real dielectric real constant (**εr**) is highly dependent on (n^2) due to the small value of (k^2). In Figure 4.12 we notice the value of (**εr**) starts to increase and then starts to decrease with increasing wavelength. Figure 4.13 shows the imaginary dielectric constant, which is sometimes called the dielectric loss coefficient, which refers to the amount of loss in the energy of the electromagnetic wave when its electrical component tries to direct the dipoles in the material towards the projecting field of the wave, as we note that the behavior of the imaginary dielectric constant is somewhat similar to the behavior of the electromagnetic wave.

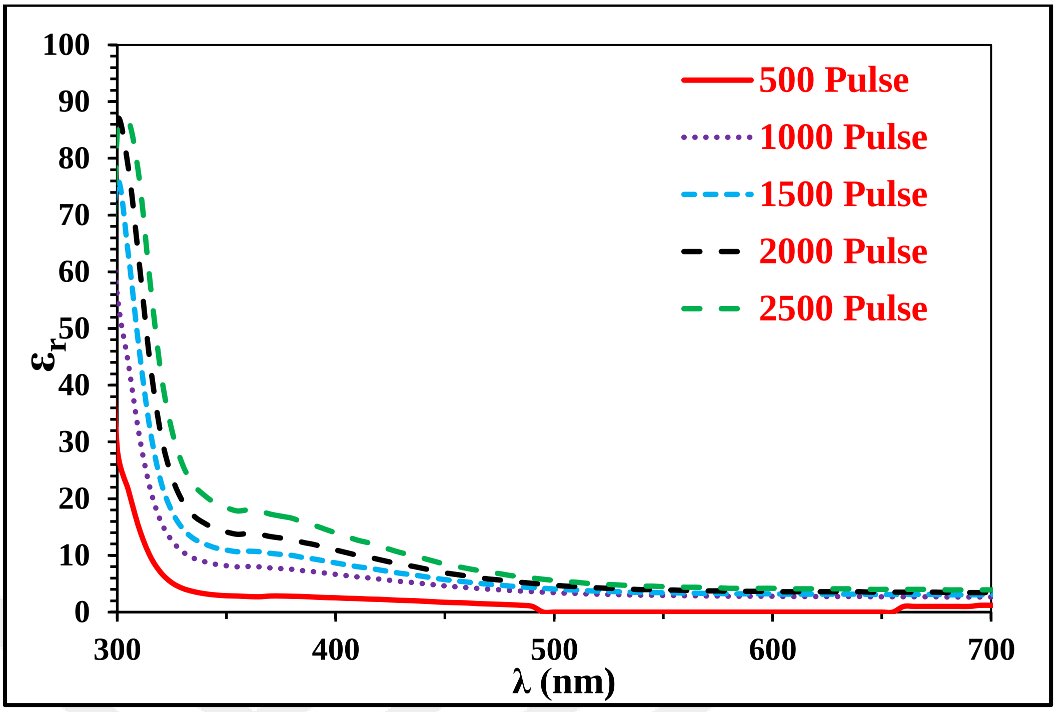

Figure 4.12 Real part of dielectric constant (εr) of Ge nanoparticles with different laser pulse numbers (500, 1000, 1500, 2000, 2500)

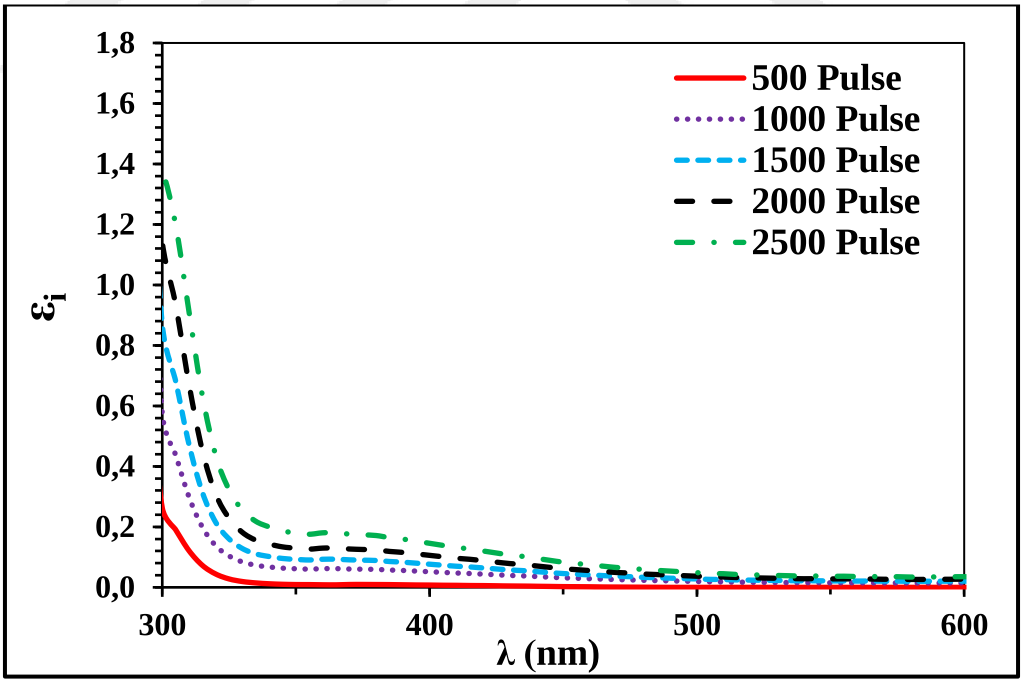

Figure 4.13 Imaginory part of dielectric constant (εi) of Ge nanoparticles with different laser pulse numbers (500, 1000, 1500, 2000, 2500)

4.3 FESEM Measurement of Ge Structures

The morphologies character of prepared Ge nanoparticles was evaluated by FESEM measurement, Figure 4.14, Figure 4.15, Figure 4.16, Figure 4.17 and Figure 4.18 shows the microscopic images of Ge nanoparticles of different pulsed laser numbers (500, 1000, 1500, 2000, and 2500) pulses, the obtained images reveals that the particle size of prepared Ge nanoparticles is variable and is within the range of (15−274) nm. The average particle sizes are (106, 140.9, 87.6, 81.68, and 117 nm) pulsed laser numbers (500, 1000, 1500, 2000, 2500) respectively. The results suggest that germanium nanoparticles aggregate into huge, irregular clusters during the production process. This is because the nanoparticles' surface atoms become unstable at high surface energies and huge surface areas, causing the particles to cluster together. The agglomeration results from the surface atoms of the particles banding together through covalent interactions to stabilize the system.

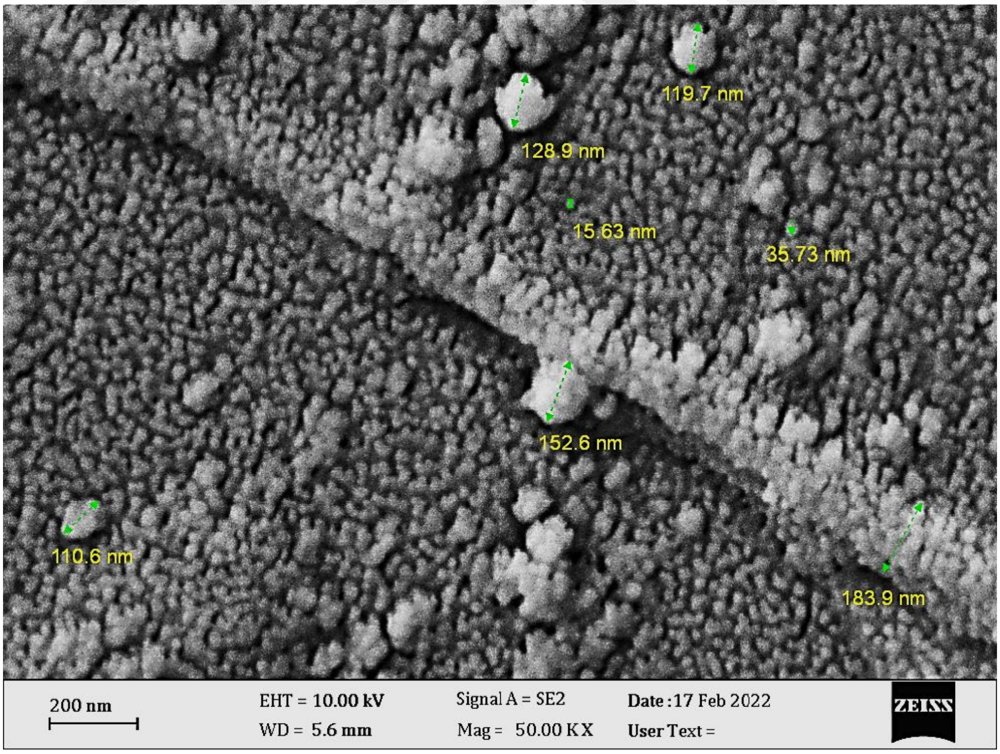

Figure 4.14 The microscopic images of Ge nanoparticles of 500 pulsed

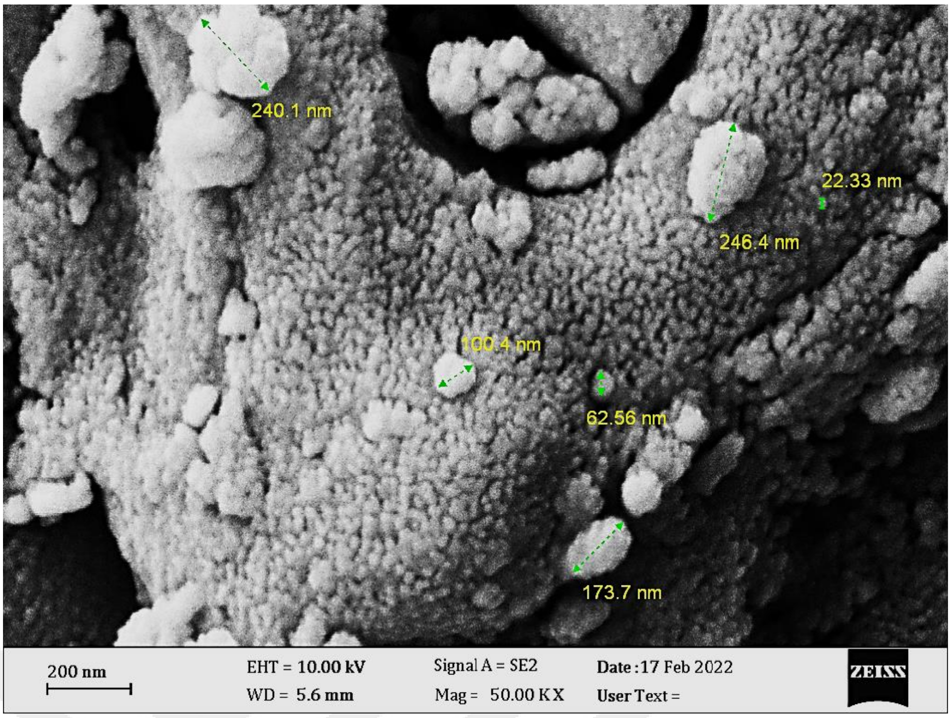

Figure 4.15 The microscopic images of Ge nanoparticles of 1000 pulsed

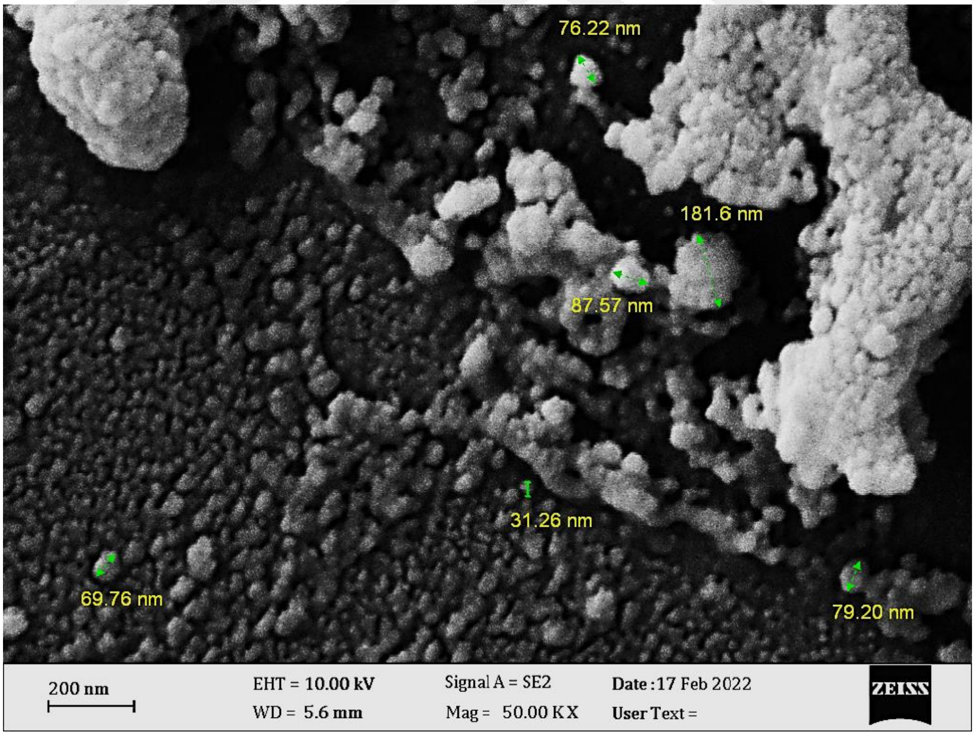

Figure 4.16 The microscopic images of Ge nanoparticles of 1500 pulsed

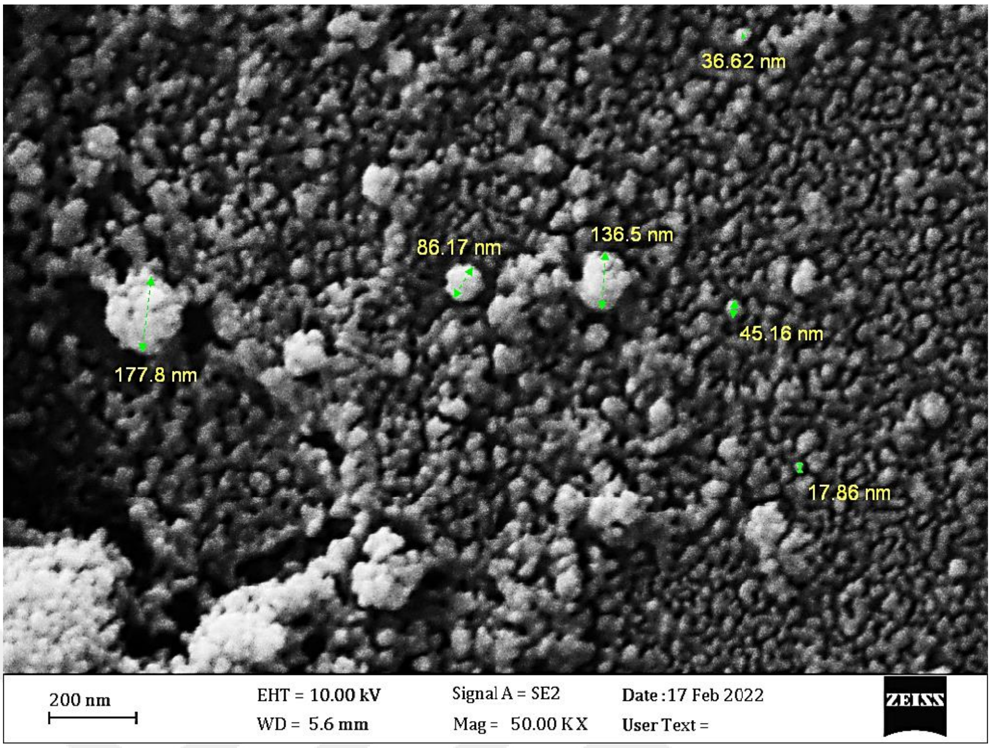

Figure 4.17 The microscopic images of Ge nanoparticles of 2000 pulsed

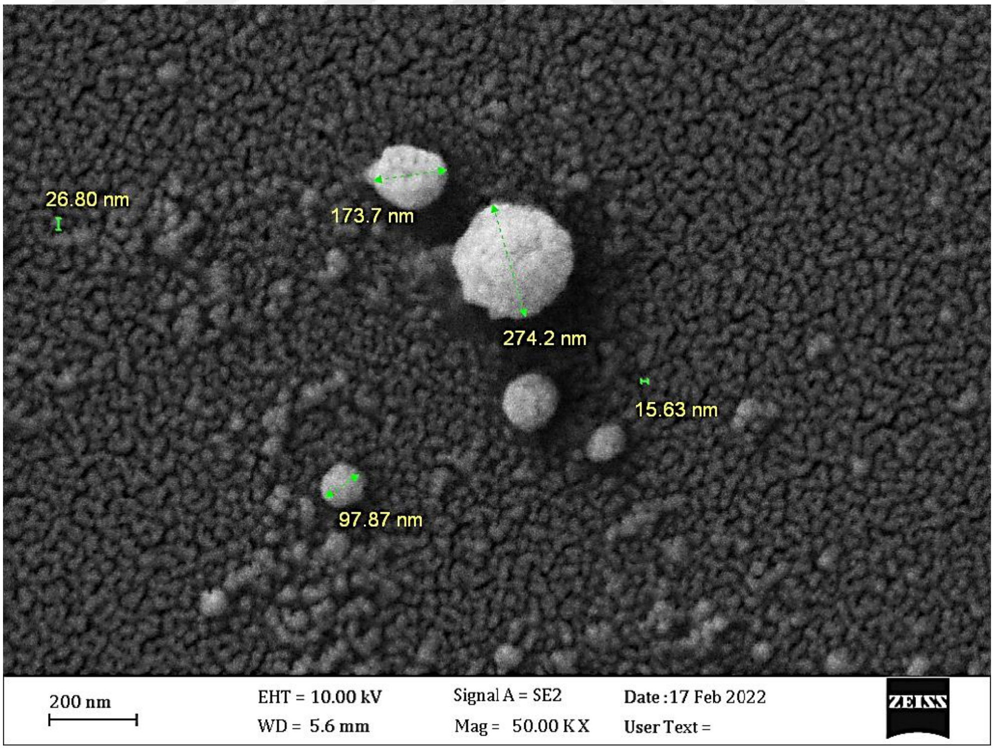

Figure 4.18 The microscopic images of Ge nanoparticles of 2500 pulsed

4.4 Gas Sensor Results

By subjecting the sensor to 149.66 ppm for a series of pulses (500, 1000, 1500, 2000, 2500) based on different temperatures (50, and 100) °C as a function of time with an on/off gas valve, we were able to determine the effect of the concentrations on the sensitivity of the sensor.

Since the adsorption process increases due to an increase in the surrounding oxygen atoms, which act as traps for electrons, the mechanical action of the sensor is caused by charge transfer between the sensing layer and the adsorbent gas, resulting in a decrease in resistance (increased current) due to a change in the particle size.

A rise in electric current (a decrease in resistance) was seen when hydrogen gas was introduced, as is the case with most N-type metal oxide semiconductors. The electric current in germanium oxide films, as a function of exposure duration to hydrogen gas at a concentration of 149.66 ppm and different numbers of Pulses, as depicted in Figure 4.19, Figure 4.20, Figure 4.21, Figure 4.22 and Figure 4.23.

From the data, it is apparent that all the produced membranes exhibited the same pattern of increased electric current value when exposed to hydrogen gas. It was also noted that the sensor's sensitivity grew with an increase in the number of pulses, as the value of the current rose. Using the Equation (2.1), we were able to determine the sensitivity of the processed films. According to Table 4.3, the sensitivity of the germanium dioxide sensor increased with the number of pulses from 500 to 2000, with the highest sensitivity value ranging from 1.17% with a response time of 19 seconds and the recovery time of 8 seconds in case 500 pulses to (13.2%) with a response time of 22 seconds and the recovery time of 13 seconds in case 2000 pulses. An increase in crystal size, which affects the adsorption process of the gas on the surface and thus the sensor's response, is responsible for this loss in sensitivity at a sample size of 2500 pulses. The surface reaction is enhanced by the presence of adsorption sites, active sites, and oxygen vacancies, all of which increase as the size of the crystals decreases.

The findings of the sensitivity showed that increasing the operating temperature from 50 to 100 °C increased the sensitivity, with the maximum value being at a few pulses of 2,000 pulses and the minimum value being at a number of pulses of 500 pulses. The activation energy at this temperature may be sufficient to complete the chemical reaction and increase the surface reaction rate of the gas, which is a major factor in the increased sensitivity of materials towards the gas as the operating temperature is raised.

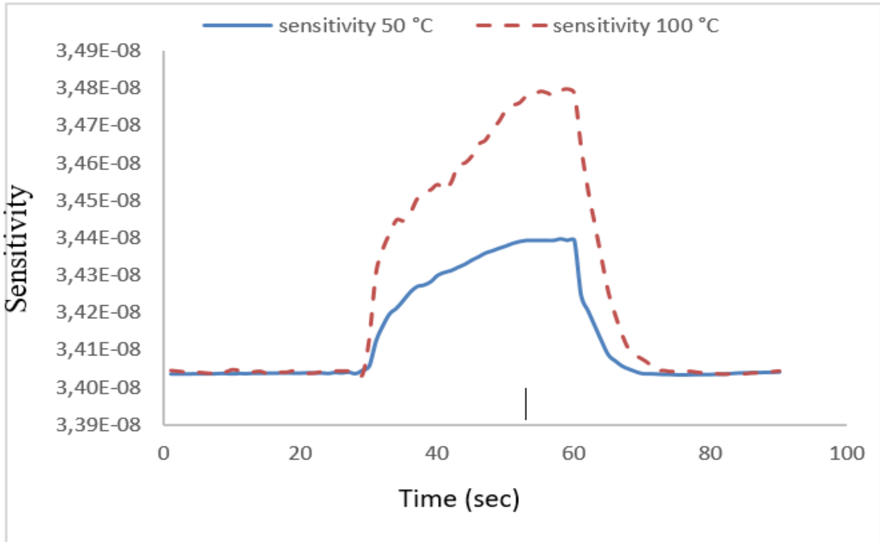

Figure 4.19 Change of sensitivity as a function of time at 500 pulses at temperatures of 50 and 100°C

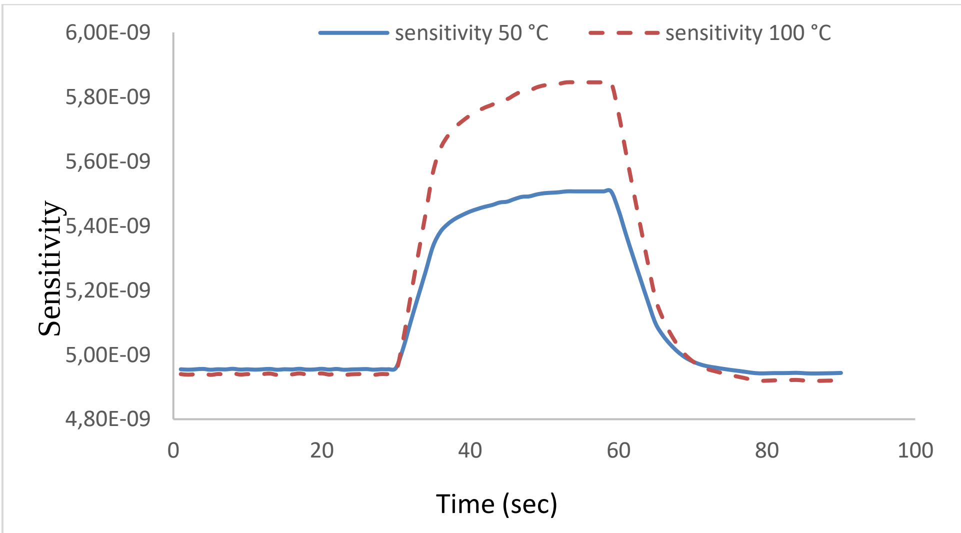

Figure 4.20 Change of sensitivity as a function of time at 1000 pulse at temperatures of 50 and 100°C

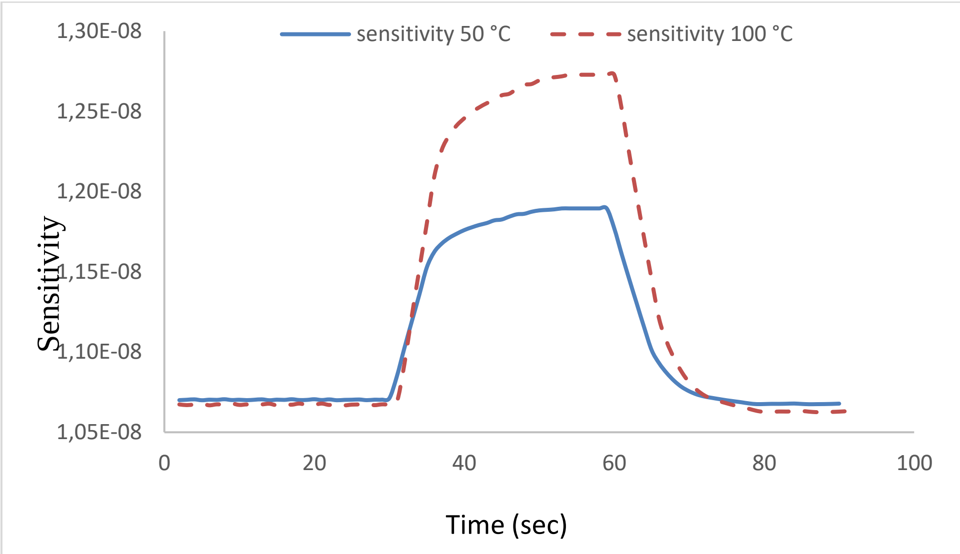

Figure 4.21 Change of sensitivity as a function of time at 1500 pulse at temperatures of 50 and 100°C

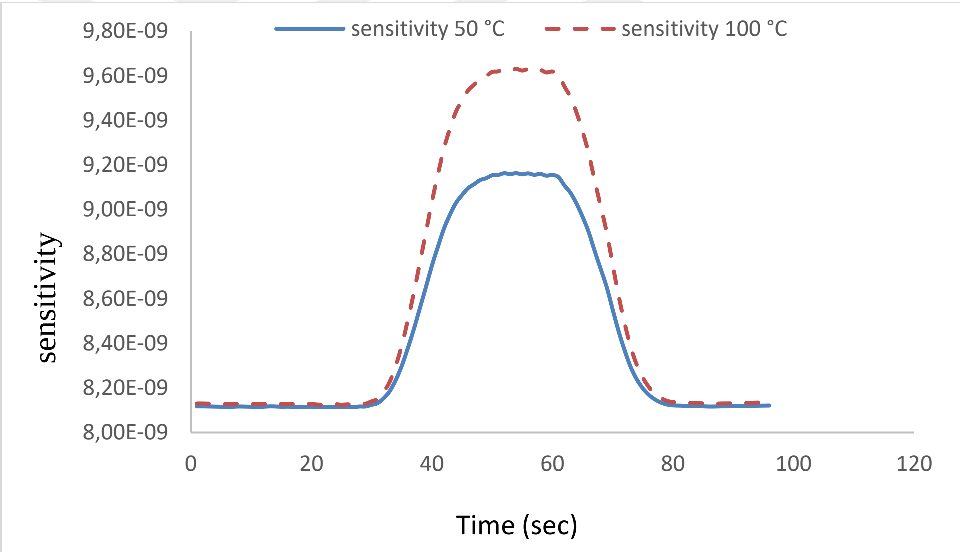

Figure 4.22 Change of sensitivity as a function of time at 2000 pulse at temperatures of 50 and 100°C

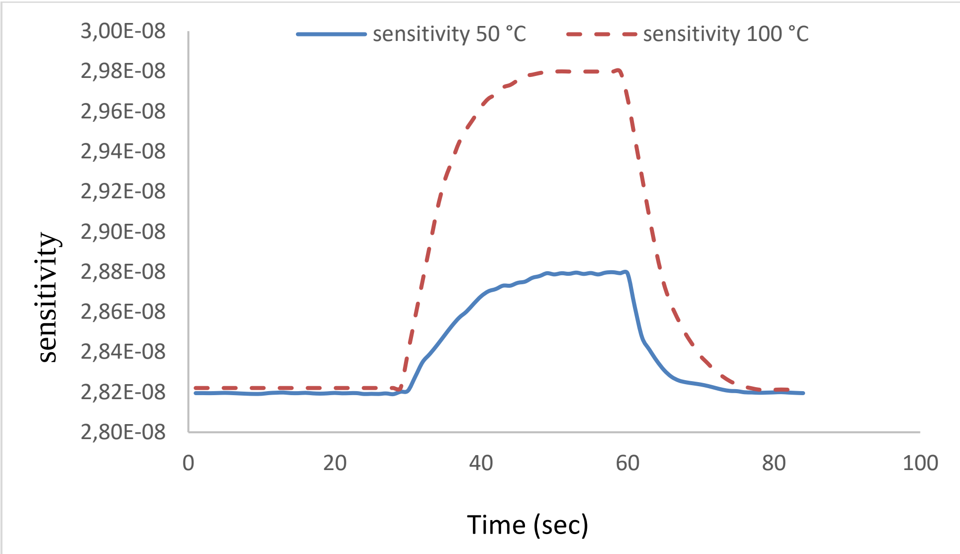

Figure 4.23 Change of sensitivity as a function of time at 2500 pulse at temperatures of 50 and 100°C

Table 4.3 Values of sensitivity, response, and recovery time

Sample	**Temperature (T)**	**Sensitivity (S)**	**Response time (Res)**	**Recovery time (Rec)**
500	50°C	1.17	19	8
1000		11.1	16	5
1500		12.68	20	11
2000		13.20	22	13
2500		2.49	21	12
500	100°C	2.05	22	12
1000		18.18	21	12
1500		18.47	22	13
2000		19.81	20	10
2500		5.31	23	17

Figure 4.24 displays the sensor's sensitivity as a function of the number of pulses, showing that at 50 and 100°C, the sensitivity increases with the number of pulses but decreases at 2500 pulses due to an increase in crystalline size. This is because the smaller the particulate size, the higher the specific surface area, the number of adsorption sites, and the surface reactant's ability to bind to the surface.Response time is depicted in Figure 4.25, and recovery time is depicted in Figure 4.26, both in terms of the number of pulses

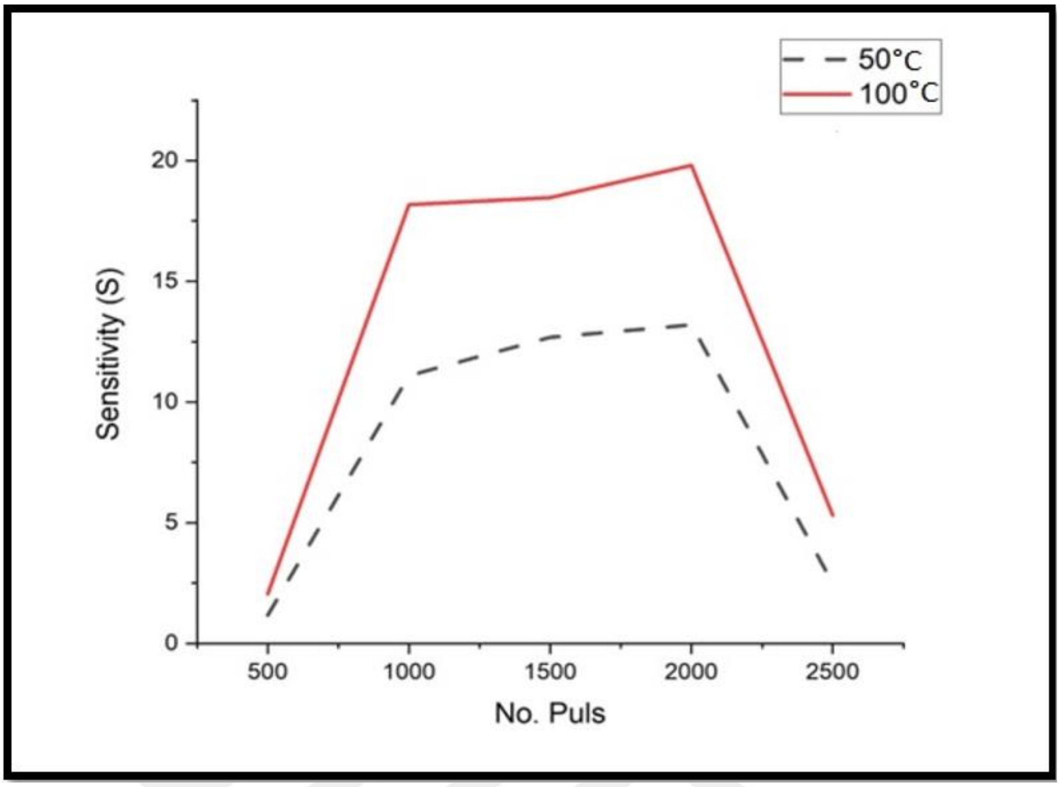

Figure 4.24 Sensitivity as a function of the number of the pulse at temperatures of 50 and 100°C

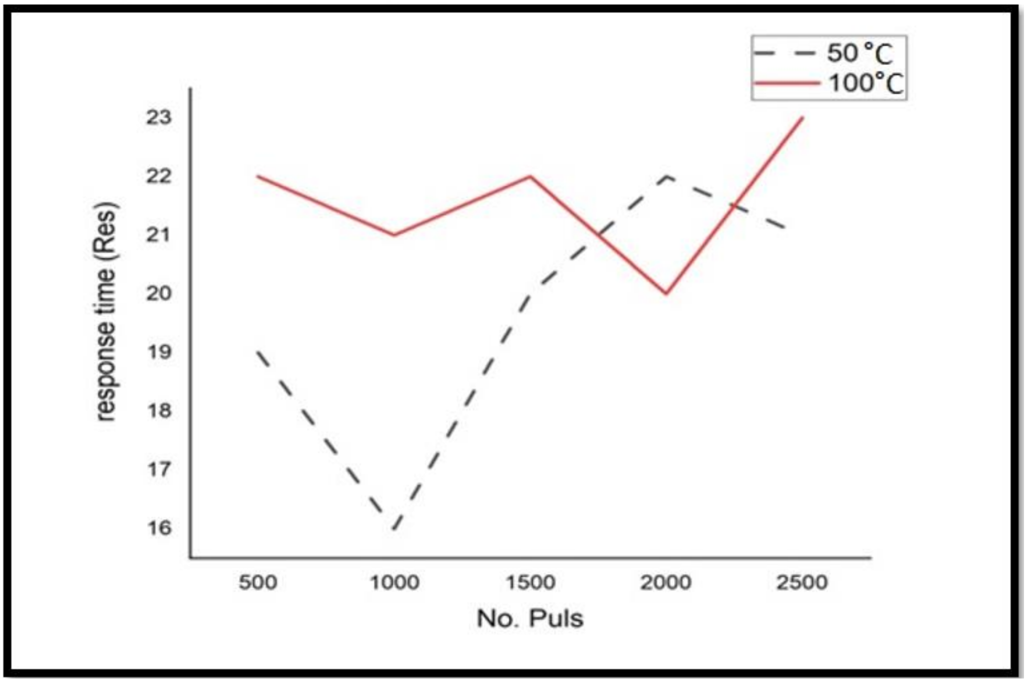

Figure 4.25 Response time as a function of the number of pulses at temperatures of 50 and 100°C

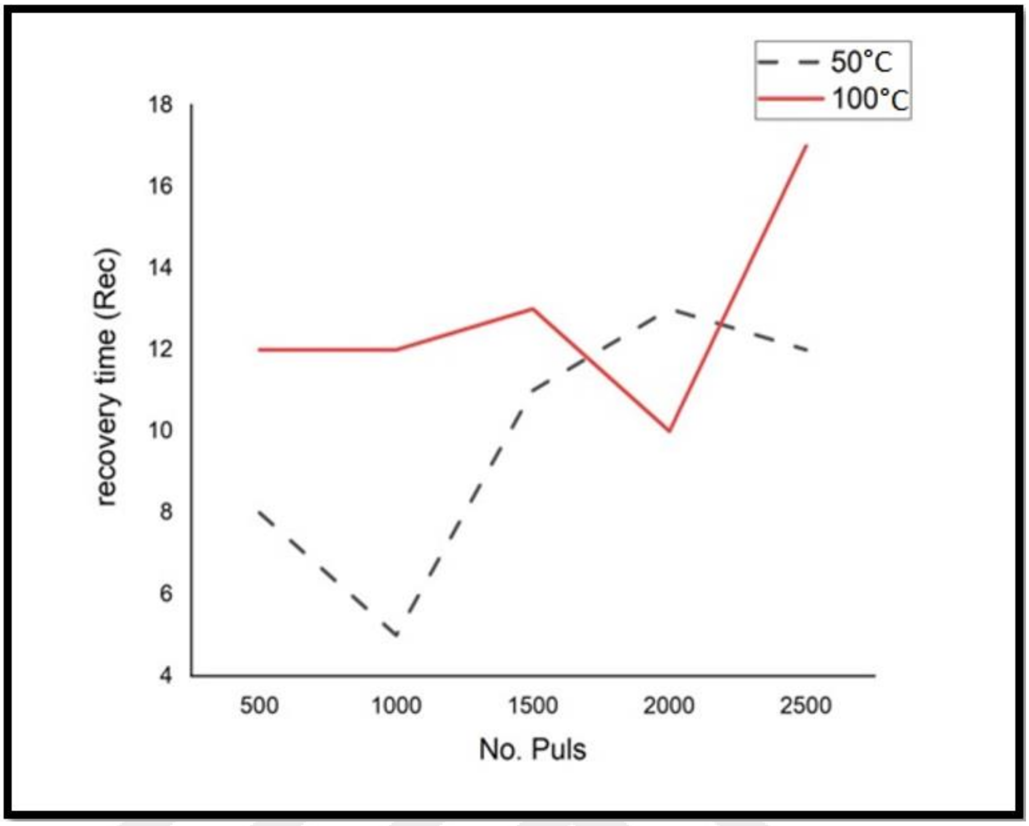

Figure 4.26 Recovery time as a function of a number of pulses at temperatures of 50 and 100°C

5. CONCLUSIONS AND RECOMMENDATION

5.1 Conclusions

Toxic gas sensors are instruments used to detect and quantify hazardous gas levels in the atmosphere. These sensors are commonly used in industrial and commercial settings where there is a risk of exposure to harmful gases. The sensor works by detecting the presence of the gas and providing an alert or warning when the concentration reaches a dangerous level. In this study, the properties of germanium thin films deposited on quartz and N-type silicon bases obtained by pulsed laser method were studied with an energy of 2 joules and with different pulses (500, 1000, 1500, 2000 and 2500) pulses. In addition to the sensitivity properties at a gas concentration of 149. and different operating temperatures of 50 and 100°C. X-ray diffraction study showed that all XRD patterns with different numbers have crystallized very well. There are three diffraction peaks of (2θ=54.67, 56.44, and 61.80), corresponding to the crystalline planes (202, 210, and 113) these peaks are related to GeO_2, these diffractions related to hexagonal structure with (ICSD 98-063-7456), addition, we can observe additional new diffraction peaks related to Ge_2O_4 at (2θ=47.84, 66.63) corresponding to the plane (120, 002), these diffractions are related to orthorhombic structure with (COD 96-900-6860). Diffraction peaks related to Germanium Oxide with structure Orthorhombic structure. Field emission scanning electron microscopy FESEM showed that the particle sizes ranged between 15-274 nm and the average particle sizes are (106, 140.9, 87.6, 81.68, and 117 nm) pulsed laser numbers (500, 1000, 1500, 2000, and 2500) respectively., and the synthesis of germanium nanoparticles revealed agglomeration of large and irregularly shaped particles. The optical properties of germanium dioxide films were also studied by measuring the absorbance and transmittance (UV-vis) spectrum within the wavelength range (300-900) nanometers showed that the spectra exhibit an apeak centered at around 300 nm. the absorption increases with the increase of laser pulse number, there was a low value at 500 pulses and a high value at 2500 pulses. As for the hydrogen gas sensor manufactured on a silicon base of type N of type 111, the electric current value of the prepared membranes increased when exposed to hydrogen gas, which is a uniform behavior for all the prepared membranes. It was also observed that the value of the current increased as the number of pulses increased, indicating that the sensor's sensitivity increased as the number of pulses increased. That increasing the number of pulses from 500 to 2000 led to an increase in sensitivity and the sensor had the greatest sensitivity value from 1.17% with a response time of 19 seconds and a recovery time of 8 seconds in case 500 pulses to (13.2%) with a response time of 22 seconds and the recovery time is 13 seconds in case 2000 pulses, while increasing the number of pulses to 2500 pulses decreased the sensitivity value to 2.49% with a response time of 19 seconds and a recovery time of 8. Consequently, we can conclude as follows:

- FESEM images showed the structure of crystal sizes at the nanoscale with hexagonal and ortrhombic structures.
- The sensitivity towards hydrogen gas increases with the increase in the number of pulses, and the best sensitivity value was obtained at the number of pulses of 2000 Pulses.

It was found that the sensitivity increases with the increase in temperature, as greater values are observed than is at 100 °C compared to what it is at 50°C.

5.2 Recommendation

- Examining the optical, structural, optical, and electrical properties of germanium films deposited on a variety of substrates including ceramics and polymers.
- Using other gases to investigate the chemical gas sensor properties of germanium films.
- Deposition of germanium films with different impurities using the pulsed laser technique with different energies with a different number of pulses to apply a gas sensor.

REFERENCES

Al-Dahan, Z. T. and Abduljabbar, L. M. 2013. Fabrication of Germanium detectors by using Nd-YAG laser. Al-Nahrain Journal for Engineering Sciences, 16(2): 168-179.

Ali, A. K. 2010. Preparation of Ag and Au nanoparticles by Pulsed Laser Ablation in liquid. PhD. Thesis, University of Technology, 189 page, Baghdad.

Al-Maher, M. M., Al-Barhawi, N. I. and Al-Jubbori, M. A. 2021. Study the effect of gamma ray on silver nanoparticles prepared by pulse laser ablation in liquid technique (PLAL). Journal of Education and Science, 30(2): 128-137.

Amendola, V. and Meneghetti, M. 2013. What controls the composition and the structure of nanomaterials generated by laser ablation in liquid solution?. Physical Chemistry Chemical Physics, 15(9): 3027-3046.

Avarmaa, K., Klemettinen, L., O'Brien, H., Taskinen, P. and Jokilaakso, A. 2019. Critical metals Ga, Ge and In: Experimental evidence for smelter recovery improvements. Minerals, 9(6): 367.

Bajaj, G. and Soni, R. K. 2009. Effect of liquid medium on size and shape of nanoparticles prepared by pulsed laser ablation of tin. Applied Physics A, 97: 481-487.

Barcikowski, S., Devesa, F. and Moldenhauer, K. 2009. Impact and structure of literature on nanoparticle generation by laser ablation in liquids. Journal of Nanoparticle Research, 11: 1883-1893.

Barrett, C. R., Nix, W. D. and Tetelman, A. S. 1973. The principles of engineering materials. Prentice-Hall, 328-348.

Barsan, N. and Weimar, U. 2001. Conduction model of metal oxide gas sensors. Journal of Electroceramics, 7: 143-167.

Bertin, E. P. 2012. Principles and practice of X-ray spectrometric analysis. Springer Science & Business Media, 1080 page, Berlin.

Bott, A. W. 1998. Electrochemistry of semiconductors. Current Separations, 17: 87-92.

Boucherif, A., Beaudin, G., Aimez, V. and Ares, R. 2013. Mesoporous germanium morphology transformation for lift-off process and substrate re-use. Applied Physics Letters, 102(1): 5-9.

Bowen, D. K. and Tanner, B. K. 1998. High resolution X-ray diffractometry and topography. CRC press, 252 page, Boca Raton.

Chen, J. 2010. Highly Sensitive and selective gas sensors based on vertically aligned metal oxide nanowire arrays. PhD. Thesis, 126 page, Universtity of New Orleans, New Orleans.

Chiu, H. W., Kauzlarich, S. M. and Sutter, E. 2006. Thermal behavior and film formation from an organogermanium polymer/nanoparticle precursor. Langmuir, 22(12): 5455-5458.

Crisp, D., Pathare, A. and Ewell, R. C. 2004. The performance of gallium arsenide/germanium solar cells at the Martian surface. Acta Astronautica, 54(2): 83-101.

Dahl, J. A., Maddux, B. L. and Hutchison, J. E. 2007. Toward greener nanosynthesis. Chemical Reviews, 107(6): 2228-2269.

Darwish, A. M., Eisa, W. H., Shabaka, A. A. and Talaat, M. H. 2016. Investigation of factors affecting the synthesis of nano-cadmium sulfide by pulsed laser ablation in liquid environment. Spectrochimica Acta Part A: Molecular and Biomolecular Spectroscopy, 153: 315-320.

Davydov, S. Y. 2005. Simple models of hydrogen adsorption on germanium. Technical Physics, 50: 110-112.

Desnica, U. V., Buljan, M., Dubcek, P., Siketic, Z., Radovic, I. B., Bernstorff, S. and Turan, R. A. T. 2006. Ion beam synthesis and characterization of Ge nanoparticles in SiO2. Nuclear Instruments and Methods in Physics Research Section B: Beam Interactions with Materials and Atoms, 249(1): 843-846.

Diehl, R., Prantzos, N. and Von Ballmoos, P. 2006. Astrophysical constraints from gamma-ray spectroscopy. Nuclear Physics A, 777: 70-97.

Dong, L., Zheng, P., Yang, Y., Zhang, M., Xue, Z., Wang, Z. and Di, Z. 2018. NO2 gas sensor based on graphene decorated with Ge quantum dots. Nanotechnology, 30(7): 074004.

Eranna, G. 2011. Metal oxide nanostructures as gas sensing devices. CRC Press, 336 page, Boca Raton.

Fang, L., Kulkarni, S., Alhooshani, K. and Malik, A. 2007. Germania-based, sol− gel hybrid organic− inorganic coatings for capillary microextraction and gas chromatography. Analytical Chemistry, 79(24): 9441-9451.

Filipponi, L. and Sutherland, D. 2013. Nanotechnologies: principles, applications, implications and hands-on activities. Publications Office of the European Union, 13(1): 1-9.

Fine, G. F., Cavanagh, L. M., Afonja, A. and Binions, R. 2010. Metal oxide semi-conductor gas sensors in environmental monitoring. Sensors, 10(6): 5469-5502.

Fishburn, J. M., Withford, M. J., Coutts, D. W. and Piper, J. A. 2006. Study of the fluence dependent interplay between laser induced material removal mechanisms in metals: Vaporization, melt displacement and melt ejection. Applied Surface Science, 252(14): 5182-5188.

Franke, M. E., Koplin, T. J. and Simon, U. 2006. Metal and metal oxide nanoparticles in chemiresistors: does the nanoscale matter?. Small, 2(1): 36-50.

Franklin, S. R. and Thareja, R. K. 2005. Simulation of cluster formation in laser-ablated silicon plumes. Journal of Applied Physics, 97(12): 2-4.

Froelich, P. N. and Andreae, M. O. 1981. The marine geochemistry of germanium: Ekasilicon. Science, 213(4504): 205-207.

Geological, S. 2008. Germanium—statistics and information. US Geological Survey, 8(2).

Ghosh, B., Sakka, Y. and Shirahata, N. 2013. Efficient green-luminescent germanium nanocrystals. Journal of Materials Chemistry A, 1(11): 3747-3751.

Goldstein, J. I., Newbury, D. E., Michael, J. R., Ritchie, N. W., Scott, J. H. J. and Joy, D. C. 2017. Scanning electron microscopy and X-ray microanalysis. Springer, 550 page, New York.

Hadi, I. H. 2015. An investigation of Germanium properties prepared by Laser Ablation in liquid. Engineering and Technology Journal, 33(8): 1-3.

Hasan, B. A., Jamal, M. R. and Ali, I. M. 2016. Sensing properties of (In2O3: Eu) thin films. Australian Journal of Basic and Applied Sciences, 10(8): 143-150.

He, C., Sasaki, T., Shimizu, Y. and Koshizaki, N. 2008. Synthesis of ZnO nanoparticles using nanosecond pulsed laser ablation in aqueous media and their self-assembly towards spindle-like ZnO aggregates. Applied Surface Science, 254(7): 2196-2202.

Hirose, K., Kakuyama, K., Murata, M., Adachi, M., Yamamoto, Y. and Takeuchi, T. Cooling-free infrared sensors with original Nanostructured Si-Ge thermoelectric material. Sumitomo Electric Technical Review, 92(1): 90-98.

Huang, J., Ye, Z. and Wang, L. 2002. A novel technique to grow Ge quantum dots on porous Si by ultrahigh vacuum chemical vapor deposition. Journal of Materials Science Letters, 21(2): 129-131.

Jumidali, M. M., Hashim, M. R. and Al-Heuseen, K. 2013. Analysis of the properties of germanium/zinc silicate film growth through a simple thermal evaporation technique for hydrogen gas sensing and deep UV photodetector application. Materials Science in Semiconductor Processing, 16(5): 1360-1364.

Kazakevich, P. V., Simakin, A. V., Voronov, V. V. and Shafeev, G. A. 2006. Laser induced synthesis of nanoparticles in liquids. Applied Surface Science, 252(13): 4373-4380.

Khanna, V. K. 2016. Integrated nanoelectronics. Nanoscience and Technology, 10: 978-81.

Khoudro, A. and Najeeb, S. H. 2020. Studying the infrared spectroscopy of the SnO2: Sb (x= 0.00, 0.01) powders. The Journal of Chemistry and Materials Research, 10: 9-16.

Korotčenkov, G. S. 2013. Handbook of gas sensor materials: Properties, advantages and shortcomings for applications. Conventional Approaches. Springer, 442 page, New York.

Kroening, K. K., Easter, R. N., Richardson, D. D., Willison, S. A. and Caruso, J. A. 2011. Analysis of chemical warfare degradation products. John Wiley & Sons, 160 page, New York.

Lassesson, A., Schulze, M., Van Lith, J. and Brown, S. A. 2007. Tin oxide nanocluster hydrogen and ammonia sensors. Nanotechnology, 19(1): 015502.

Lehn, J. M. 1993. Supramolecular chemistry—molecular information and the design of supramolecular materials. In Makromolekulare Chemie. Macromolecular Symposia. Basel: Hüthig & Wepf Verlag, 69(1): 1-17.

Lettington, A. H. 1998. Applications of diamond-like carbon thin films. Carbon, 36(6): 555-560.

Li, Y. T., Zhang, J., Teng, H., Li, K., Peng, X. Y., Jin, Z. and Yu, Q. Z. 2003. Blast waves produced by interactions of femtosecond laser pulses with water. Physical Review E, 67(5): 056403.

Link, S. and El-Sayed, M. A. 1999. Size and temperature dependence of the plasmon absorption of colloidal gold nanoparticles. The Journal of Physical Chemistry B, 103(21): 4212-4217.

Liu, C. 2005. A study of particle generation during laser ablation with applications. PhD. Thesis, University of California, 155 page, Berkeley.

Mackenzie, D. M. A. and Brown, S. A. 2012. Germanium nano-cluster films as humidity and hydrogen sensors. Journal of Applied Physics, 112(7).

Maeda, M. 1984. Laser dyes: properties of organic compounds for dye lasers. Academic Press, 225 page, Cambridge.

Maeda, Y. 1995. Visible photoluminescence from nanocrystallite Ge embedded in a glassy SiO 2 matrix: evidence in support of the quantum-confinement mechanism. Physical Review B, 51(3): 1658.

Mandayo, G. G., Castano, E., Gracia, F. J., Cirera, A., Cornet, A. and Morante, J. R. 2003. Strategies to enhance the carbon monoxide sensitivity of tin oxide thin films. Sensors and Actuators B: Chemical, 95(1): 90-96.

Mays, A. H. 2016. Rare earth additive effect on sensing behavior of ZnO/PS nanostructure. MSc. Thesis, Anbar University, 87 page, Anbar.

Melcher, F. and Buchholz, P. 2014. Germanium. Critical Metals Handbook, 177-203.

Morris, J. and Willis, J. 2007. Whitepaper on nanotechnology. EPA, 1-136.

Narayanan Pradeep, R. 2021. Design and study of Hybrid DNA nanostructures and complex 3D DNA materials. PhD. Thesis, Arizona State University, 224 page, Tempe.

Naskar, S., Freytag, A., Deutsch, J., Wendt, N., Behrens, P., Köckritz, A. and Bigall, N. C. 2017. Porous aerogels from shape-controlled metal nanoparticles directly from nonpolar colloidal solution. Chemistry of Materials, 29(21): 9208-9217.

Noël, S., Axente, E. and Hermann, J. 2009. Investigation of plumes produced by material ablation with two time-delayed femtosecond laser pulses. Applied Surface Science, 255(24): 9738-9741.

Ozdemir, S. 2011. Formation, characterization, and flow dynamics of nanostructure modified sensitive and selective gas sensors based on porous silicon. Georgia Institute of Technology, 589 page, Atlanta.

Park, C. O. and Akbar, S. A. 2003. Ceramics for chemical sensing. Journal of Materials Science, 38: 4611-4637.

Pasanen, T. P., Isometsä, J., Garin, M., Chen, K., Vähänissi, V. and Savin, H. 2020. Nanostructured germanium with> 99% absorption at 300–1600 nm wavelengths. Advanced Optical Materials, 8(11): 2000047.

Patel, A. K., Pandey, K., Agrawal, S., Pandey, N. and Bajpai, R. 2019. Crystalline and absorption studies on cadmium sulphide doped polycarbonate composite. In AIP Conference Proceedings. AIP Publishing, 2100(1): 7-12.

Povarnitsyn, M. E., Itina, T. E., Khishchenko, K. V. and Levashov, P. R. 2009. Suppression of ablation in femtosecond double-pulse experiments. Physical Review Letters, 103(19): 195002.

Prabakar, S., Shiohara, A., Hanada, S., Fujioka, K., Yamamoto, K. and Tilley, R. D. 2010. Size controlled synthesis of germanium nanocrystals by hydride reducing agents and their biological applications. Chemistry of Materials, 22(2): 482-486.

Rieke, G. H. 2007. Infrared detector arrays for astronomy. Annual Review of Astronomy and Astrophysics, 45: 77-115.

Röck, F., Barsan, N. and Weimar, U. 2008. Electronic nose: Current status and future trends. Chemical Reviews, 108(2): 705-725.

Samà, J., Domènech-Gil, G., Gràcia, I., Santander, J., Cané, C., Seifner, M. and Romano-Rodríguez, A. 2016. Site-selectively grown p-type Ge NWs as a gas sensor. Procedia Engineering, 168: 1056-1060.

Shen, C., Trypiniotis, T., Lee, K. Y., Holmes, S. N., Mansell, R., Husain, M. and Barnes, C. H. 2010. Spin transport in germanium at room temperature. Applied Physics Letters, 97(16).

Shieh, J., Chen, H. L., Ko, T. S., Cheng, H. C. and Chu, T. C. 2004. Nanoparticle-assisted growth of porous Germanium thin films. Advanced Materials, 16(13): 1121-1124.

Shimizu, Y. and Egashira, M. 1999. Basic aspects and challenges of semiconductor gas sensors. MRS Bulletin, 24(6): 18-24.

Siu, C. 2022. Semiconductor physics. In Electronic Devices, Circuits, and Applications. Springer International Publishing, 35-39.

Szweda, R. 2005. Germanium phoenix. III-Vs Review, 18(7): 55.

Tribble, A. 2002. Electrical Engineering materials and devices. PhD. Thesis, University of Iowa, 242 page, Iowa.

Trindade, T., O'Brien, P. and Pickett, N. L. 2001. Nanocrystalline semiconductors: synthesis, properties, and perspectives. Chemistry of Materials, 13(11): 3843-3858.

Tsuji, T., Thang, D. H., Okazaki, Y., Nakanishi, M., Tsuboi, Y. and Tsuji, M. 2008. Preparation of silver nanoparticles by laser ablation in polyvinylpyrrolidone solutions. Applied Surface Science, 254(16): 5224-5230.

Vadavalli, S., Valligatla, S., Neelamraju, B., Dar, M. H., Chiasera, A., Ferrari, M. and Desai, N. R. 2014. Optical properties of germanium nanoparticles synthesized by pulsed laser ablation in acetone. Frontiers in Physics, 2: 5-7.

Vinod, M. and Gopchandran, K. G. 2015. Ag@ Au core–shell nanoparticles synthesized by pulsed laser ablation in water: effect of plasmon coupling and their SERS performance. Spectrochimica Acta Part A: Molecular and Biomolecular Spectroscopy, 149: 913-919.

Wang, J. B., Zhang, C. Y., Zhong, X. L. and Yang, G. W. 2002. Cubic and hexagonal structures of diamond nanocrystals formed upon pulsed laser induced liquid–solid interfacial reaction. Chemical Physics Letters, 361(1-2): 86-90.

Wang, S. G., Tan, C. J., Yang, Q., Xu, Y. X., Li, S. L. and Chen, X. P. 2017. A novel ultra-sensitive nitrogen dioxide sensor based on germanium monosulfide monolayer. IEEE Electron Device Letters, 38(11): 1590-1593.

Washio, K. 2003. SiGe HBT and BiCMOS technologies for optical transmission and wireless communication systems. IEEE Transactions on Electron Devices, 50(3): 656-668.

Wei, L., Lin-Li, Z. and Xiao-Jing, Z. 2009. Grain size effect on electrical conductivity and giant magnetoresistance of bulk magnetic polycrystals. Chinese Physics Letters, 26(11): 117502.

Willardson, R. K., Beer, A. C., Pankove, J. I. and Johnson, N. M. 1991. Hydrogen in semiconductors. Semiconductors and Semimetals, 61.

Xiao, J., Liu, P., Wang, C. X. and Yang, G. W. 2017. External field-assisted laser ablation in liquid: An efficient strategy for nanocrystal synthesis and nanostructure assembly. Progress in Materials Science, 87: 140-220.

Yoon, H. R., Jo, W., Lee, E. H., Lee, J. H., Kim, M., Lee, K. Y. and Khang, Y. 2005. Generation of phase-change Ge–Sb–Te nanoparticles by pulsed laser ablation. Journal of Non-Crystalline Solids, 351(43-45): 3430-3434.

Yunusa, Z., Hamidon, M. N., Kaiser, A. and Awang, Z. 2014. Gas sensors: A review. Sensor Transducers, 168(4): 61-75.

Zeng, H., Cai, W., Li, Y., Hu, J. and Liu, P. 2005. Composition/structural evolution and optical properties of ZnO/Zn nanoparticles by laser ablation in liquid media. The Journal of Physical Chemistry B, 109(39): 18260-18266.

Zhakhovskii, V. V., Inogamov, N. A., Petrov, Y. V., Ashitkov, S. I. and Nishihara, K. 2009. Molecular dynamics simulation of femtosecond ablation and spallation with different interatomic potentials. Applied Surface Science, 255(24): 9592-9596.

Zhang, J. Z. 2009. Optical properties and spectroscopy of nanomaterials. World Scientific, 400 page, Singapore.

Zhang, J., Claverie, J., Chaker, M. and Ma, D. 2017. Colloidal metal nanoparticles prepared by laser ablation and their applications. ChemPhysChem, 18(9): 986-1006.

Zhao, Y., Li, S., Zeng, Y. and Jiang, Y. 2015. Synthesis and properties of Ag/ZnO core/shell nanostructures prepared by excimer laser ablation in liquid. APL Materials, 3(8): 1-7.

Zhigilei, L. V., Lin, Z. and Ivanov, D. S. 2009. Atomistic modeling of short pulse laser ablation of metals: connections between melting, spallation, and phase explosion. The Journal of Physical Chemistry C, 113(27): 11892-11906.

Zimmer, K. 2009. Analytical solution of the laser-induced temperature distribution across internal material interfaces. International Journal of Heat and Mass Transfer, 52(2): 497-503.